DYNAMICAL MODELING OF

A THREE-DIMENSIONAL SPIN LIQUID

by

Shu Zhang

A dissertation submitted to The Johns Hopkins University in conformity with the requirements for the degree of Doctor of Philosophy.

Baltimore, Maryland

August, 2019

Abstract

A spin liquid is a magnetic phase of matter distinctively different from conventional ordered magnets. It does not develop any long-range magnetic order even in the zero temperature limit. Theoretical models have predicted various exotic features in their ground states and excitations. The quest for spin liquids in real materials has been focusing on synthesizing compounds close to known spin liquid models and identifying relevant features in of their excitations.

$NaCaNi_2F_7$ is an almost ideal realization of the Heisenberg pyrochlore antiferromagnet, which is a model for a three-dimensional classical spin liquid. It is also a system of $S = 1$ spins, where quantum effects are nonnegligible.

We utilize classical and semi-classical models for spin dynamics to study the excitation spectrum of $NaCaNi_2F_7$ and find the results in good agreement with inelastic neutron scattering experiments. The agreement can be understood by a combined picture of the statistics of spin wave excitations and the exploration of the system among many degenerate ground states. Our approaches can also be applied to other candidate compounds for classical spin liquids, $MgCr_2O_4$ as a known example.

ABSTRACT

Primary Reader: Oleg Tchernyshyov

Secondary Reader: Collin Broholm

Acknowledgments

Foremost, I wound like to express my sincere gratitude to my thesis advisor Oleg Tchernyshyov, without whose guidance and support my journey in theoretical physics would not have started. Some of my most enjoyable time during the graduate school was spent in his classroom lectures and office mini-lectures. His knowledge and vision keep inspiring me.

I would also like to especially thank Collin Broholm, who is my first year advisor, a member of my thesis advisory committee and the supervisor for many of my projects, and Roderich Moessner, who has supervised the main work presented in my dissertation, for sharing their knowledge and passion with me.

I appreciate the collaboration with Hitesh Changlani, Kemp Plumb, Allen Scheie, Jon Leiner, and the discussion with Ibou Bah, Yi Li and Ari Turner. I learned a lot from every one of them. I also thank all the faculty members in my research exam committee, graduate board oral exam committee and thesis defense committee for their advises.

In addition, I am grateful for the experience at the Kavli Institute for Theoretical

ACKNOWLEDGMENTS

Physics, which broadened my interest in physics. I also thank Se Kwon Kim for his hospitality at the University of Missouri, where most of this dissertation was written.

Finally, I would like to thank my dear friends and colleagues in the department. Special thanks go to Sayak Dasgupata, who has been sharing all my joy and sorrow of being a young researcher. I also deeply thank Joseph Monti, Jonathan Gaudet and Canon Sun among many others, who made a wonderful part of my life.

Contents

List of Tables

List of Figures

Chapter 1

Introduction

In dealing with macroscopic objects composed of $\sim 10^{23}$ atoms or molecules, physicists have always managed to start the investigation by working with fewer degrees of freedom, one way or another. This is the most natural for non-interacting systems, for example, the ideal gas. In statistical mechanics, we start with the partition function z_1 of a single atom with the Boltzmann distribution according to its kinetic energy. Therefore the partition function of the entire system with N identical atoms is the Nth power of that of one atom z_1^N. Extensive quantities that are proportional to the system size N, such as energy and entropy, can be calculated simply based on the property of a single atom.

For interacting systems, the picture does not come as easily. Luckily, when working at a low enough temperature, not all degrees of freedom in a system are active. In the limit of zero temperature, the ground state, which minimize the total energy, is

ordinarily unique. At least, that is what the third law of thermodynamics tells us. Thus, finding the ground state is a primary question in studying phases of matter. At finite temperatures, the description of excitations can sometimes be simplified to a model of effectively non-interacting quasiparticles, which brings back the convenience in considering non-interacting systems. However, even finding the ground state or a quasiparticle description is difficult most of the time. The few exceptional cases where this can be done are worth our special attention.

1.1 Conventional magnetic orders

Magnetism studies materials with magnetic dipoles, where exchange interactions between spins of magnetic atoms originates from the Coulomb interaction between their electrons. A classical spin can be viewed as a three-component vector $\mathbf{s} = S\hat{\mathbf{n}}$, where S is the spin length and $\hat{\mathbf{n}}$ is the unit vector along the direction the spin is pointing. Different types of interactions between them lead to distinct material properties.

The result of interactions in selecting a unique ground state is easily visualized in a simple ferromagnet. All spins are aligned in the same direction, resulting in a large total magnetic moment. Thus the magnetization $\mathbf{m}$, defined as magnetic moment per unit volume, can be used as an order parameter, distinguishing the ferromagnetically ordered state from the disordered paramagnetic state.

In a Heisenberg model of the ferromagnet, $H = J\sum_{\langle ij\rangle} \mathbf{s}_i \cdot \mathbf{s}_j$, where $J < 0$ and $\mathbf{s}_i$ and $\mathbf{s}_j$ are spins located at nearest-neighbor sites $\mathbf{r}_i$ and $\mathbf{r}_j$. The Hamiltonian has a global rotational symmetry, which is spontaneously broken by the ground state with a specific orientation of the total moment.

The $J < 0$ interaction favors an antiferromagnetic order, where spins alternate between one orientation and its opposite. It was observed in materials much later than ferromagnet, because of its vanishing magnetization. Instead, we can define a staggered order parameter as the magnetization of one sublattice subtracted by the other $\mathbf{n} = (\mathbf{m_1} - \mathbf{m_2})/2$. Other ordered states with non-collinear or even non-coplanar spins in a unit cell, can be identified with more complicated order parameters.

The magnetic interactions do not necessarily lead to a long-range magnetic order in a material. Thermal or quantum fluctuations can sometimes effectively destroy long-range orders. For example, the Mermin-Wagner theorem states that spontaneously breaking of continuous symmetry cannot happen at finite temperature for systems in one or two dimensions. As we shall see later for some systems, quantum tunneling also works in its own way to prevent long-range order, which turns out to be an

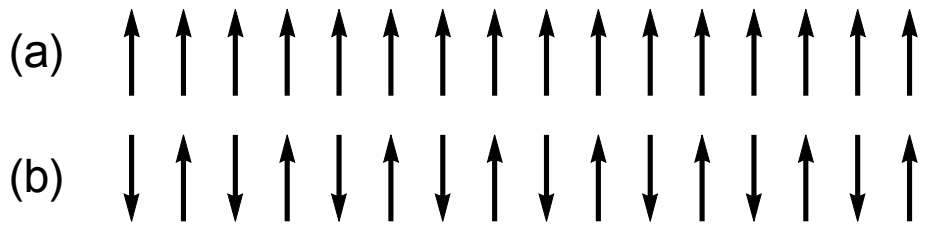

Figure 1.1: Ferromagnetic and antiferromagnetic states on a one-dimensional spin chain.

interesting subject to study. Here we remark that whether a magnetically interacting spin system develops long-range order or not, it is fundamentally different from a non-interacting paramagnet. The short-range magnetic correlations can also drive different magnetic behavior. An important idea is the local exchange field.

1.2 Local exchange field

Consider a typical non-interacting paramagnet polarized by an external magnetic field. Its magnetization is (in the lowest order approximation) directly proportional to the field and inversely proportional to the temperature $\mathbf{m} = (C/T)\mathbf{B}$, where C is the Curie constant depending on the material. This gives the susceptibility of the system $\chi = m/H = m\mu_0/B = C/T$.

For interacting spins, the magnetic field acting locally on a spin is corrected by its environment—the neighboring spins, $B \to B + \lambda m = m\mu_0/(C/T)$, where where λ is the Weiss molecular field constant. The susceptibility thus has a different dependence on the temperature

$$\chi = \frac{C}{T - \frac{\lambda C}{\mu_0}}. \tag{1.1}$$

This is the Curie-Weiss law for interacting magnets in the paramagnetic region. For ferromagnetic interactions, $\lambda > 0$, the environment provides a correction aligned with the spin locally. The susceptibility diverges at the temperature $\theta_{CW} = |\lambda|C/\mu_0$, where the transition from the high temperature paramagnetic phase to the low temperature

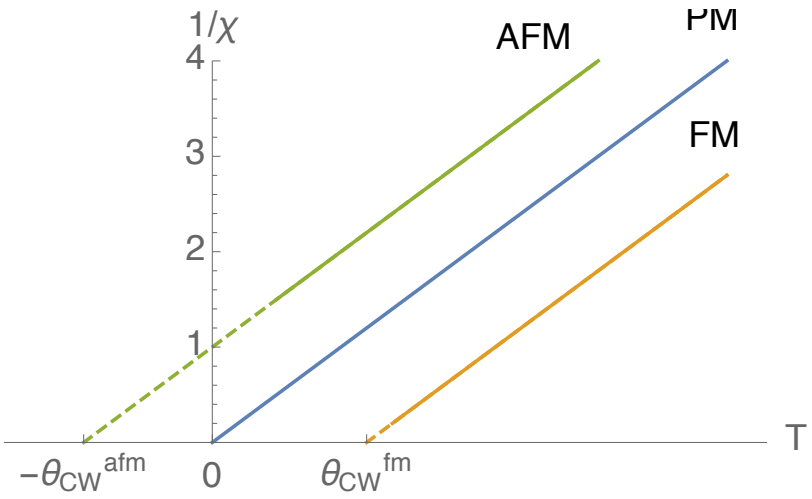

Figure 1.2: Curie-Weiss law for paramagnet (PM), ferromagnet (FM) and antiferromagnet (AFM). In a certain temperature region, the inverse susceptibility is linearly dependent on the temperature. Extrapolation gives the Curie-Weiss temperature.

ordered phase is expected. It applies similarly to a antiferromagnetic system with $\lambda < 0$, where the environment provides an opposite correction. See Figure 1.2 for a plot of the inverse susceptibility verses temperature in different systems.

More specifically, the local exchange field at a site $\mathbf{r}_i$ is defined as $\mathbf{H}_{\text{eff}} = -\partial H/\partial \mathbf{s}_i$. For the Heisenberg model, $\mathbf{H}_{\text{eff}} = -J\sum_{j\in i}\mathbf{s}_j$. The Curie-Weiss law is important because susceptibility is directly measurable in experiments. It gives as an estimation of the type and strength of the dominating magnetic interaction, even though the behavior of a system at low temperature can deviate from expectation (for example, antiferromagnetic system might order at a temperature much lower than Θ_{CW} or might not order at all). It is a reflection of the short-range spin correlation in an interacting system. A lot of other experimental techniques, such as neutron scattering, measure the wavevector- and frequency- resolved susceptibility, which yield a lot more

information about spin correlations.

The local exchange field also contributes directly to the dynamics of the spin. When a spin is not aligned with its environment, it precesses following the Landau-Lifshitz equation

$$\hbar \frac{d}{dt}\mathbf{s}_i = -\mathbf{s}_i \times \mathbf{H}_{\text{eff}}, \tag{1.2}$$

just like an angular momentum precesses under a torque. The collective precessional motions of spin deviations from the ground state are called spin waves. Their spectrum can be calculated by linearizing the classical equation of motion (1.2). For a system with long-range order, the wavevector $\mathbf{q}$ is a good quantum number because of the discrete translational symmetry. There exists a well-defined dispersion relation $\omega(\mathbf{q})$ between the energy and the wavevector of a spin wave, which can be observed as a sharp dispersive branch in spectroscopic experiments. A quantized spin wave carrying angular momentum $\hbar$ is a quasiparticle excitation called a magnon.

In the absence of magnetic order, translational symmetry is absent, so the spin waves do not have a well-defined wavevector. The eigenmodes nonetheless can be (in principle) determined, even though they have a complex spatial character [1].

As we have mentioned, an antiferromagnetic system sometimes orders at a temperature T_N (called the Néel temperature) much lower than the prediction θ_{CW}. A scenario where this behavior happens is in the presence of magnetic frustration, with the ratio $f = \theta_{CW}/T_N$ as a measure of frustration.

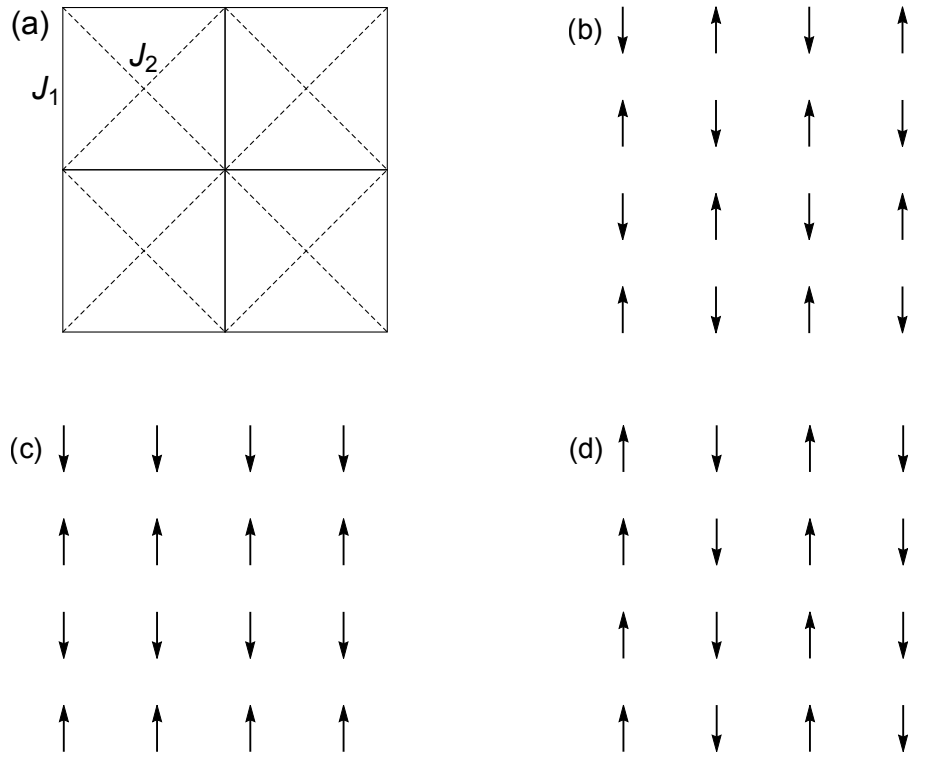

Figure 1.3: The J_1-J_2 model on a square lattice. (a) The nearest-neighbor interactions J_1 are on the solid bonds and the next-nearest-neighbor interactions J_2 are on the dashed bonds. (b) When $J_2 \ll J_1$, the ground state is the Néel state. (c,d) When $J_2 \gg J_1$, the ground state is the stripy state.

1.3 Magnetic frustration

Frustration refers to the impossibility for a spin state to simultaneously minimize all local interactions. The preference for a particular state is thus weaker, suppressing the ordering temperature. In this sense, it is quite common in natural systems.

Frustration occurs in systems with competing interactions. For example, on a square lattice with nearest-neighbor antiferromagnetic interactions J_1 only, the Néel ordered state has next-nearest neighboring spins aligned. It can be destabilized by turning on the next-nearest-neighbor antiferromagnetic interaction J_2. This is the J_1-

J_2 model on a square lattice, see Figure 1.3. When J_2 is sufficiently large, the system will end up in a stripy state where not all nearest-neighbors are anti-aligned. At the transition between the Néel order and the stripe order, the two phases compete. There is the possibility that instead of a typical phase transition, a new state of matter without either of the two orders might emerge. This way of inducing frustration is hard to achieve because the parameter range of $J_1 \sim J_2$ is very small and difficult to access by real materials.

Another way to induce frustration is by the geometry of the lattice, where it can be achieved without tuning the strength of interactions. Take the triangular lattice as an example. We consider an Ising spin-1/2 with only two states (up and down, perpendicular to the lattice plane) on each site and antiferromagnetic interactions between nearest neighbors, see Figure 1.4(a). The state of the entire system is expressed by a direct product of all individual spin states. On a single triangle, there are six ground states (one up two down and one down two up) with the same total energy. In all six states, the interaction on two bonds are minimized and one bond is frustrated.

Consider a ground state of the triangular lattice, with each triangle in one of the six ground states. After fixing the state of one triangle, some of the neighboring spins still have the freedom to be up or down. Therefore, different regions of the same lattice appear to have different spin patterns. Also, the ground states are highly degenerate.

The degeneracy here has two important features—accidental and extensive. First, they are not imposed by the symmetry of the Hamiltonian, as regions with different patterns are not related by a translation of lattice vectors. Second, as the lattice grows larger, the number of degenerate ground states Ω_{GS} grows extensively, giving a residual entropy of $S_{\mathrm{res}} = k_B \ln(\Omega_{\mathrm{GS}}) \propto N^{\alpha}$ with $\alpha = 1$ or sub-extensively with $0 < \alpha < 1$. Wannier showed that a triangular lattice of Ising spins with antiferromagnetic interactions has a residual entropy per spin $\approx 0.3383 k_B$ [2], where k_B is the Boltzmann constant. The extensive degeneracy of ground states is a defining feature of frustration.

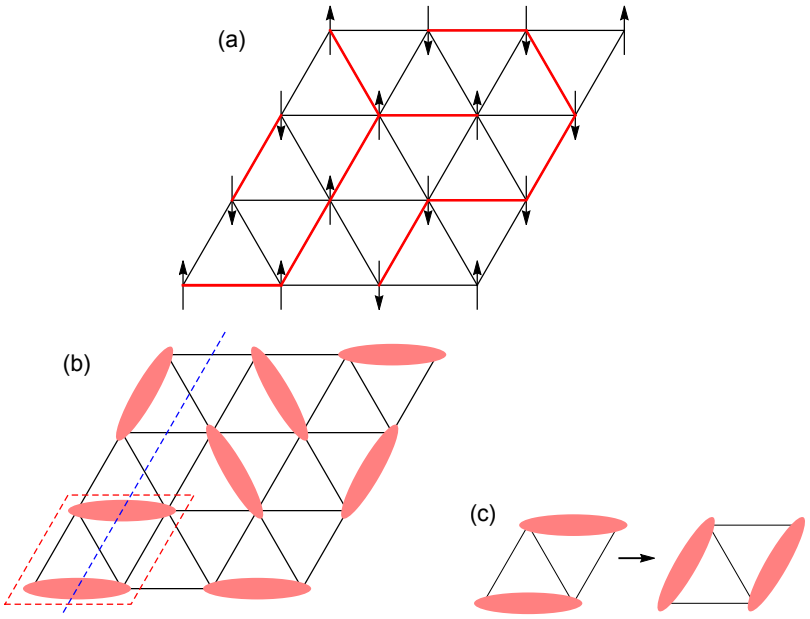

Figure 1.4: (a) Ising spins on the geometrically frustrated triangular lattice. Frustrated bonds are in red. (b) A pattern of dimerization of quantum spin-1/2 degrees of freedom. Each red ellipse is a dimer $|\uparrow\downarrow\rangle - |\downarrow\uparrow\rangle)/\sqrt{2}$. The Blue dashed line cuts through a set of the horizontal bonds. The dashed red diamond encircles a flippable plaquette. (c) Flipping a plaquette can change the dimer configuration.

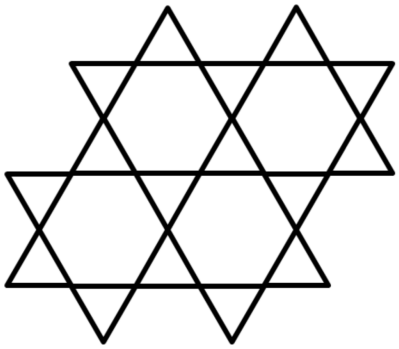

Figure 1.5: The kagome lattice made of corner-sharing triangles.

So, the triangular geometry of the lattice is very effective in frustrating spins. Even more so for the kagome lattice (corner-sharing triangles, see Figure 1.5), and the pyrochlore lattice (corner-sharing tetrahedra, described in details in Chapter 2) in three-dimensions, which is the main subject of this dissertation.

Because of the high degeneracy the the ground state, even at very low temperature, the system is not trapped at one unique state but can explore many states. It is possible that the system does not develop long range order but stays in a disordered, yet highly correlated state, like a liquid. This is the concept of a "spin liquid", it is also called cooperative paramagnet, distinguished from the non-interacting paramagnet.

1.4 Quantum spin liquids

A more interesting scenario arises when quantum fluctuations are considered. It is believed that quantum fluctuations can be the principle factor to drive the frustrated

system into an exotic phase of matter with no magnetic order down to zero temperature. This is the quantum spin liquid phase. The very first proposal for a quantum spin liquid was the resonating valence bond (RVB) state [3] based on quantum spins on a triangular lattice with antiferromagnetic interaction.

A pair of spins can form an isolated dimer, such as a singlet state, $(|\uparrow\downarrow\rangle - |\downarrow\uparrow\rangle)/\sqrt{2}$. For the antiferromagnetic Heisenberg interaction, the singlet state actually has lower the energy than any of the two product states $|\uparrow\downarrow\rangle$ and $|\downarrow\uparrow\rangle$. Thus, it is energetically favorable to form singlets across the entire triangular lattice, each spin belonging to one and only one singlet, see Figure 1.4(b). Different patterns as the result of dimerization are degenerate states. We can consider a superposition of many dimerization patterns to lower the energy even further. In the end, we end up with a single ground state composed of macroscopically many degrees of freedom, one tunneling into another, without any long-range magnetic order.

Since the RVB proposal, many other models for quantum spins liquids have been invented and intensively studied.

As of today, a complete definition of the term "quantum spin liquid" still remains a work in progress [4–7]. It is mostly based on the following features.

First, the absence of long-range magnetic order and other forms of spontaneous symemtry breaking; the latter is to exclude states such as valence bond solids, which are more or less frozen dimerized patterns.

Second, fractional excitations, usually spinons. We illustrate what they are with

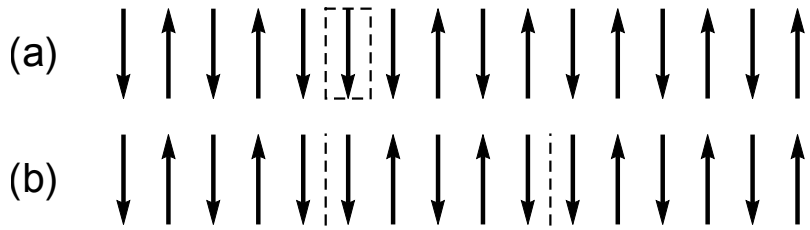

Figure 1.6: Spinons in an antiferromagnetic spin-1/2 chain. (a) One spin in the dashed box is flipped from the ground state. Two domain walls (spinons) are created. (b) They can move apart freely from each other.

two examples.

One is a domain wall in the spin-1/2 antiferromagnetic chain, see Figure 1.6. One spin flip creates two domain walls in the system. They can then move apart freely from each other. Since one spin flip changes the angular momentum by $\hbar$ and each domain wall carries half of that. A domain wall is a fractionalized excitation called a spinon.

The other example is an unpaired spin in the dimerized triangular lattice. As shown in Figure 1.7, breaking a dimer creates two free spins, which can then move apart from each other.

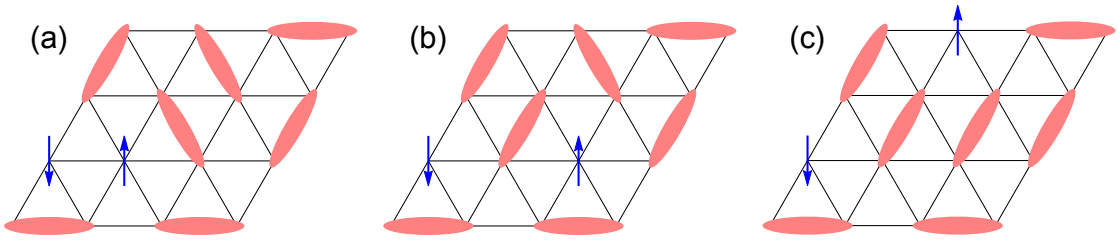

Figure 1.7: Spinons in the dimerized triangular lattice. (a) Two opposite spins are freed by breaking a dimer. (b), (c) An unpaired spin (a spinon) can propagate by breaking and reforming dimers.

Spinons are regarded as fractional excitations of a system because local operations always create or destroy two (or more) of them simultaneously.

The third feature we need to mention about quantum spin liquids is topological orders and long-range entanglement. Although quantum spin liquids cannot be characterized by conventional order parameters in the Landau theory of phase transitions, some of them possess what is known as "topological order", which is a global feature usually characterized by a topological invariant. For example, for the dimerization pattern shown in Figure 1.4(b), consider a straight line cutting through a set of parallel bonds of the triangular lattice and count the number of dimers on those bonds. We can define a quantity called the parity p and assign $p = 0$ ($p = 1$) if an even (odd) number of dimers are encoutered. The parity is a global property of the state that is invariant under any plaquette flipping.

Topological orders also often indicate nontrivial entanglement of the system. The presence of long-range entanglement is a statement that the wavefunction of the system cannot be reduced to a product state of wavefunctions in one region and its complement. The existence of these global features are important as they sharply delineate a quantum spin liquid as a phase of matter from trivially disordered states.

Unfortunately, these features are not as helpful when it comes to the search for quantum spin liquids in real materials. The identification of a quantum spin liquid state is difficult precisely because of the absence of either long-range order and spontaneous symmetry breaking. Topology and long-range quantum entanglement are

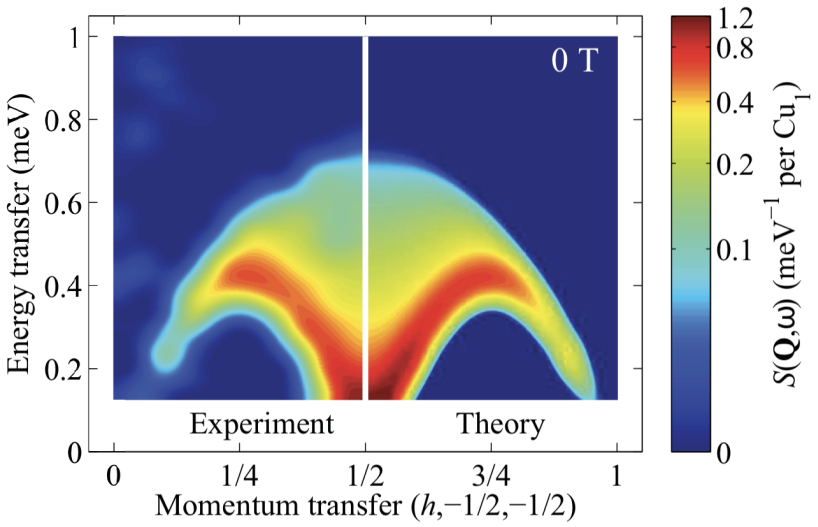

Figure 1.8: Neutron scattering results for spinon excitations in the antiferromagnetic spin-1/2 chain. The experiment is performed for $CuSO_4 \cdot 5D_2O$ in Reference [8].

rarely accessible by experimental probes. We commonly rely on measuring fractionalized excitations.

In spectroscopic experiments such as neutron and Raman scattering, local probes create two or more fractional excitations at a time. For example, in a neutron scattering experiment of an antiferromagnetic spin-1/2 chain, a neutron can transfer angular momentum $\hbar$ into the system, creating a spinon pair. Also transferred is a given amount of momentum and energy, which can be distributed in different ways between the two spinons, resulting a continuum spectrum shown in Figure 1.8.

Special transport properties of the fractional excitations carrying heat, spins or gauge charges can also serve as evidence of their existence. Although the interpolation of the experimental results are sometimes debatable, a few candidates have been agreed upon [7, 9].

1.5 Structure of dissertation

In this dissertation, we present the study of the three-dimensional spin-1 material $NaCaNi_2F_7$ as a candidate for a quantum spin liquid. For reasons outlined above, our work focuses on the understanding of its excitation spectrum. The dissertation is structured as follows. We start in Chapter 2 with an introduction to the geometrically frustrated pyrochlore lattice and the typical spin liquid models proposed for it. We deal with classical and semi-classical theories as an attempt to model the excitations and dynamics in the model of our primary interest—the perturbed antiferromagnetic Heisenberg model on a pyrochlore lattice. We discuss these approaches in Chapter 3. It turns out they work out surprisingly well in explaining the neutron scattering experiment data for $NaCaNi_2F_7$. The understanding of this agreement leads to a natural and practical picture for the spin dynamics in the system. We depict this route of understanding in detail in Chapter 4. Chapter 5 contains a discussion and concluding remarks.

Chapter 2

Pyrochlore Antiferromagnet

The geometric property of a lattice structure is fundamental in determining magnetic properties of the spins system on top of it. One of the most intensively studied lattice structure in three dimensions, on which various models yielding exotic magnetic phases have been proposed [10–13], is the pyrochlore lattice.

In this chapter, we first introduce the pyrochlore magnet and its basic properties, as direct consequences of the lattice symmetry. Then we review two typical and well-understood spin liquid models on the pyrochlore lattice, the quantum spin ice and classical spin liquid, the latter is much closely related to the research work in later chapters.

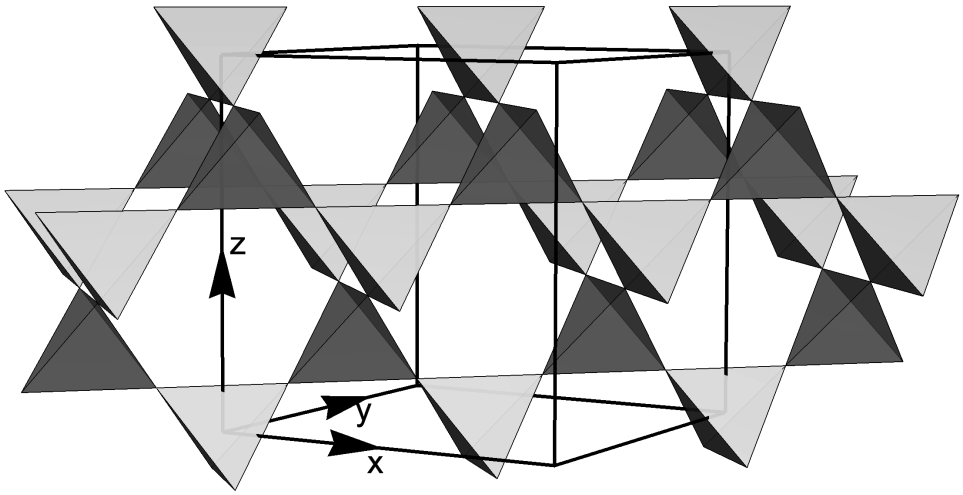

Figure 2.1: The pyrochlore lattice is a nework of corner-sharing tetrahedra. An up tetrahedron (in dark grey) and a down tetrahedron (in light grey) share the site that serves as their inversion center. Also shown are the global coordinate frame and the conventional cubic unit cell.

2.1 Pyrochlore lattice

The pyrochlore lattice is built from corner-sharing tetrahedra, as shown in Figure 2.1. Each lattice site is an inversion center and shared between an up tetrahedron and a down tetrahedron. For the down tetrahedron centered at the origin of the global reference frame, its four corners have coordinates

$$\mathbf{r}_0 = \frac{1}{8}(1,1,1), \quad \mathbf{r}_1 = \frac{1}{8}(1,-1,-1), \quad \mathbf{r}_2 = \frac{1}{8}(-1,1,-1), \quad \mathbf{r}_3 = \frac{1}{8}(-1,-1,1). \tag{2.1}$$

The full pyrochlore lattice can then be constructed from this minimal unit cell by applying translations generated by the primitive vectors of the face-centered cubic

(fcc) lattice

$$\mathbf{a}_1 = \frac{1}{2}(0,1,1), \quad \mathbf{a}_2 = \frac{1}{2}(1,0,1), \quad \mathbf{a}_3 = \frac{1}{2}(1,1,0). \tag{2.2}$$

Each of sites $\mathbf{r}_a$, $a = 0,1,2,3$ generates a fcc sublattice. It is conventional to use a larger unit cell—the cubic unit cell as shown in Figure 2.1. Its lattice constant is set to be the unit length.

2.1.1 Spin interactions

The interactions between electron spins are often dominated by Heisenberg exchange, which is isotropic in spin space. Electron orbitals can also contribute to the interaction. Relativistic corrections, such as spin-orbit couplings, become important for heavier elements. For magnetic atoms in a material, one of the consequences of the reduced symmetry is that interactions between them are less symmetric.

The most general form of a Hamiltonian describing bilinear interactions between two spins on neighboring sites $\mathbf{r}_i$ and $\mathbf{r}_j$ is

$$H_{ij} = \sum_{\mu\nu} J_{ij}^{\mu\nu} s_i^\mu s_j^\nu, \tag{2.3}$$

where Roman subscripts refer to lattice sites and Greek superscripts to Cartesian spin components ($\mu, \nu = x, y, z$). The tensor J_{ij} has 9 components. But not all of them are independent, as the exchange energy must be invariant under lattice symmetries.

We go to a local coordinate frame to illustrate this. In Figure 2.2, take the interaction J_{01} between $\mathbf{s}_0$ and $\mathbf{s}_1$ as an example. The three axes of the local frame are chosen

to be ξ, η and ζ, so that planes $\xi\zeta$ and $\eta\zeta$ are two of the mirror planes of the tetrahedron. We can then take advantage of the law of transformation for spin components under mirror reflections: components parallel to the mirror plane are antisymmetric while the perpendicular one is symmetric. Under the mirror reflection with respect to the plane $\xi\zeta$ containing the bond between $\mathbf{r}_0$ and $\mathbf{r}_1$, terms that reverse sign, namely $s_0^\xi s_1^\eta$, $s_0^\eta s_1^\xi$, $s_0^\zeta s_1^\eta$ and $s_0^\eta s_1^\zeta$, must have vanishing couplings. Hence 4 components of the interaction tensor are already ruled out. Under the mirror reflection with respect to plane $\eta\zeta$, $s_0^\xi s_1^\zeta$ transforms into $-s_0^\zeta s_1^\xi$. The coupling constants for these two terms thus must be opposite. We end up with 4 independent exchange constants in the interaction tensor. Returning to the global frame, we find the exchange tensor takes

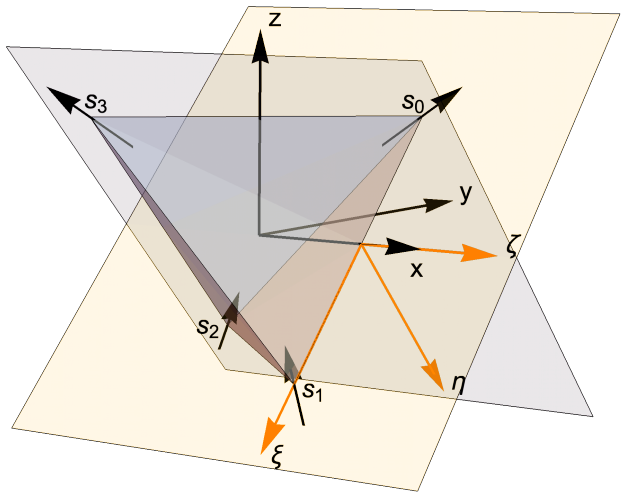

Figure 2.2: Spin interactions on a single tetrahedron. The global coordinate frame $(\mathbf{x}, \mathbf{y}, \mathbf{z})$ and the local coordinate frame $(\boldsymbol{\xi}, \boldsymbol{\eta}, \boldsymbol{\zeta})$ defined for bond b_{01}. The spin configuration is an example satisfying the ice rule.

the form

$$J_{01} = \begin{pmatrix} J_2 & J_4 & J_4 \\ -J_4 & J_1 & J_3 \\ -J_4 & J_3 & J_1 \end{pmatrix}. \tag{2.4}$$

Interactions between other pairs of spins on the tetrahedron can then be generated by three-fold rotations around the local [111] axes, which point from the center of a tetrahedron to its corners.

This symmetry analysis is only for billinear interactions between nearest neighbors. Other possible interactions, such as Zeeman coupling, single-ion anisotropy, and biquadratic interactions are neglected here.

2.1.2 Ordered states

Given a set of the four coupling constants, we are able to figure out what spin configurations on a pyrochlore lattice minimize the total exchange energy of the system. But this task is not obviously easy. Even the minimal unit cell contains four spins, hence 12 spin components, i.e. 8 degrees of freedom with the length of each spin fixed. The lattice symmetry, again, plays an important role in dividing up this large manifold and identifying different ordered patterns.

There are subsets of the manifold that are invariant under the symmetry operations of the lattice. One example is the configuration with all spins pointing inwards to or outwards from the center of the tetrahedron, see Figure 2.3 (a). This is

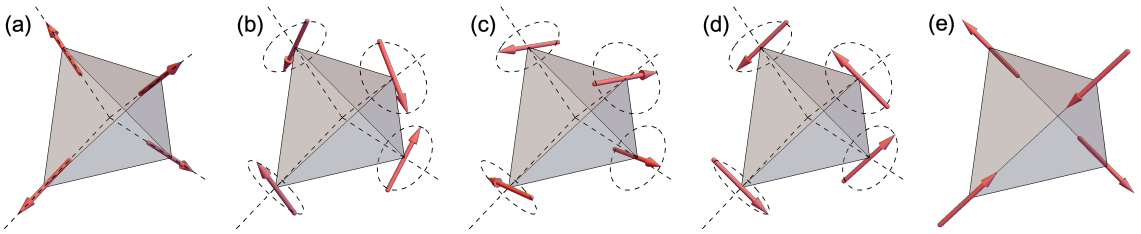

Figure 2.3: Typical ordered states on the pyrochlore lattice: (a) All-in-all-out state, (b) ψ_2 state, (c) ψ_3 state, (d) Non-collinear ferromagnetic state ψ_4, and (e) Palmer-Chalker state. The dashed lines mark the local [111] axes and the dashed circles mark the planes perpendicular to them.

called the all-in-all-out state. No symmetry operation can transform it into any other configurations. Another simple example is the collinear ferromagnet state. Under all symmetry operations, spins are always aligned and explores only inside a three-dimensional manifold. A more interesting case is the Γ_5 manifold spanned by ψ_2 and ψ_3 states shown in Figure 2.3 (b) and (c). This is a one dimensional manifold where ψ_2 and continuously transform into ψ_3 by rotating all spins around their local [111] axes by the same angle. The non-collinear ferromagnet state and the Palmer-Chalker state are also shown Figure 2.3(d) and (e), each belonging to a three-dimensional invariant manifold. These configurations are the typical magnetic ordered states on a pyrochlore lattice. We refer to Appendix A for their order parameters.

2.2 Spin ice

A general consideration of spin states on a pyrochlore lattice has turned out to be complicated. In this section, we look into a simple but interesting situation consider-

ing only one spin component.

In some rare-earth pyrochlore materials, such as $Ho_2Ti_2O_7$ [14] and $Dy_2Ti_2O_7$ [15], due to a strong single-ion anisotropy, the magnetic moments are constrained to point along the local [111] axes. We define the local $\mathbf{z}$ axis on a site as the unit vector pointing from the center of the down tetrahedron to the center of the up tetrahedron, the two of which share the site, as shown in Figure 2.4. Therefore the spins are Ising like, they only take two values $+\mathbf{z}$ and $-\mathbf{z}$.

We consider the simplified spin Hamiltonian

$$H_{\text{Ising}} = -J_I \sum_{\langle ij \rangle} \sigma_i \sigma_j (\mathbf{z}_i \cdot \mathbf{z}_j), \tag{2.5}$$

where $\langle ij \rangle$ denotes a pair of nearest neighbors, $\sigma_i = \pm 1$ and $\mathbf{z}_i \cdot \mathbf{z}_j = -1/3$ for $i \neq j$.

For antiferromagnetic coupling in the global frame, $J_I < 0$ between local spin components. This case is unfrustrated. The Hamiltonian $H_{\text{Ising}} = (J_I/3) \sum_{\langle ij \rangle} \sigma_i \sigma_j = (J_I/6) \sum_{\boxtimes} (\sum_{i \in \boxtimes} \sigma_i)^2 + \text{const.}$ is perfectly minimized by the all-in-all-out state shown

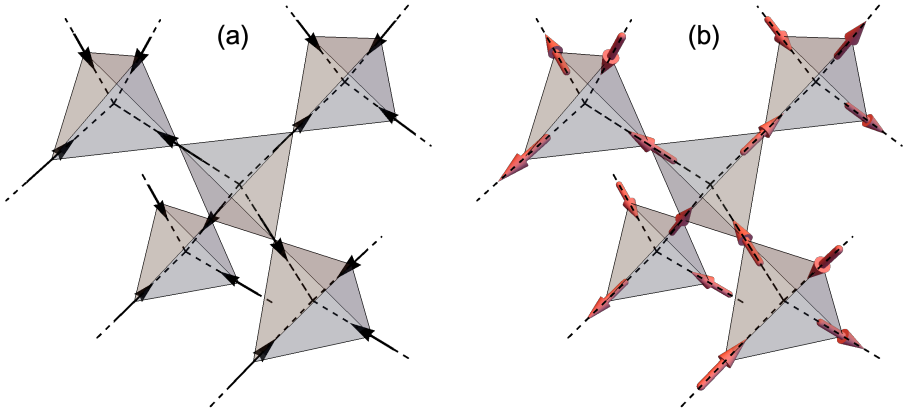

Figure 2.4: (a) Local z axes defined on lattice sites. The center tetrahedron is a down tetrahedron. (b) A spin ice configuration that satisfies two-in-two-out rule.

in Figure 2.3 (a). The ground state has a long-range magnetic order, all spins are $+\mathbf{z}$ or all $-\mathbf{z}$.

For $J_I > 0$, not all bonds can be in the low energy state. The total exchange energy on a tetrahedron is minimized by a "two-in-two-out" spin configuration (two spins aligned with the local z axis and two anti-aligned, see Figure 2.4 (b)). There are 6 states on a single tetrahedron that satisfy the "two-in-two-out" rule. In analogy with the configurations of Hydrogen positions in a molecule of water ice, the system is named the spin ice [11].

There is a net moment on the tetrahedron, reflecting the ferromangetic nature of the spin interaction in the global frame. But the entire system does not have a ferromagnetic order. Notably, fixing the spin configuration on one tetrahedron does not eliminating different options for its neighboring tetrahedra. Like the antiferromagnetically interacting Ising spins on a triangular lattice, the spin ice ground states are extensively degenerate. The system is disordered.

2.2.1 Quantum spin ice

An important model for quantum spin liquid is proposed on top of these considerations of the spin ice. Quantum fluctuations are turned on by adding a small local interaction.

$$H_{\mathrm{XXZ}} = \sum_{\langle ij \rangle} \left[J_z s_i^z s_j^z + \frac{J_\perp}{2} (s_i^+ s_j^- + \mathrm{h.c.}) \right] \tag{2.6}$$

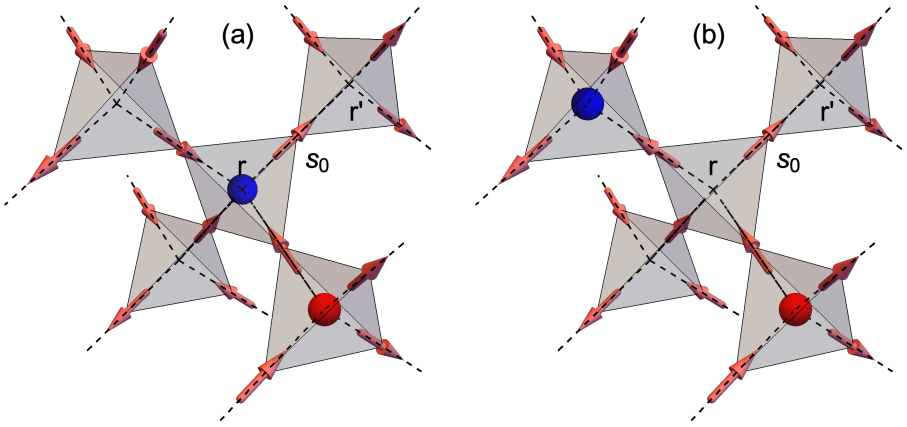

Figure 2.5: Charge excitations in a quantum spin ice. (a) A pair of positive (red) and negative (blue) charges are created by a spin flipping. (b) They can propagate apart along the path of spin flips.

where $s_i^{\pm} = s_i^x \pm i s_i^y$ and s_i^z are components in the local frame with local $\mathbf{z}$ axis defined previously.

This is the XXZ model for quantum spin ice [16], In the limit where $J_\perp$ is much smaller than J_z (weak quantum fluctuations of spins), the ground state is known to be a quantum spin liquid of a specific type: its low-energy description is reminiscent of a U(1) gauge theory. The term $U(1)$ refer to a variable on a circle parametrized by an angular variable between 0 and 2π. A well-known example of a $U(1)$ gauge theory is Maxwell's electrodynamics, the theory of the electromagnetic field. Here, we briefly illustrate the excitations in quantum spin ice in the language of lattice quantum electrodynamics.

We label tetrahedra by the coordinates of their centers on the diamond lattice, see Figure 2.5. The bipartite diamond lattice allows us to define oriented link variables $E_{\mathbf{r}\mathbf{r}'} = -E_{\mathbf{r}'\mathbf{r}} = s_i^z$, where the pyrochlore site i is shared by tetrahedra $\mathbf{r}$ and $\mathbf{r}'$.

The sum of Ising spins on a tetrahedron translates into the (lattice version of) the divergence of an electric field, $\sum_{i\in\mathbf{r}} s_i^z = (\mathrm{div}\, E)_\mathbf{r} = e_\mathbf{r}$. This can be interpreted as the Gauss law for "electric charges", which are quantized by definition. A tetrahedron satisfying the ice rule has $e_\mathbf{r} = 0$. A "one-in-three-out" state and a "three-in-one-out" state have electron charge $+1$ and -1 respectively. Because the ground state is a charge vacuum, electric charges are excitations of the system.

To make the electric field $E_{\mathbf{rr}'}$ dynamical, we need its canonical conjugate, the gauge potential $A_{\mathbf{rr}'}$. In quantum mechanics, $A_{\mathbf{rr}'}$ acts like a coordinate and $E_{\mathbf{rr}'}$ as its momentum. Acting with $\exp(iA_{\mathbf{rr}'})$ on a quantum state shifts $E_{\mathbf{rr}'}$ by a unit, effectively flipping the spin. The discrete eigenvalues of momentum E suggest that coordinate $A_{\mathbf{rr}'}$ is cyclic: the wavefunction has periodic boundary conditions, $\psi(A_{\mathbf{rr}'} + 2\pi) = \psi(A_{\mathbf{rr}'})$, hence the terminology $U(1)$ gauge theory.

Given the gauge field, we can define the magnetic field as its curl and deduce the existence of "magnetic monopoles" and "photons", just as in quantum electrodynamics [16, 17].

A fluctuation of one spin flip from the ground state creates two opposite charges on the neighboring tetrahedra, see Figure 2.5 (a). The charge can then propagate by flipping another spin to recover the ice rule on the tetrahedron it occupies, as shown in Figure 2.5. After they are created, electric charges interact weakly (compared to the energy cost to create them) through the gauge field. Separating them to infinitely far from each other only costs finite amount of energy, thus a pair of charge excitations

are not tightly bound to each other. The system is thus said to be in a deconfined phase [5, 16].

It has been shown that [18, 19] a deconfined $U(1)$ phase does not exist in two dimensions. In this sense, the three-dimensional pyrochlore antiferromagnets bear particular interest in the search for quantum spin liquids.

2.3 Heisenberg pyrochlore antiferromagnet

Now we release the constraints of Ising spins and recover the full spherical symmetry of classical spins. With isotropic interactions for all spin components, we have the antiferromagnetic Heisenberg model on a pyrochlore lattice.

$$H_{\text{Heisenberg}} = J_H \sum_{\langle ij \rangle} \mathbf{s}_i \cdot \mathbf{s}_j, \tag{2.7}$$

where $J_H > 0$. It is a typical example where the macroscopic degeneracy of the ground states, as a result of geometric frustration, prevent the system from developing a magnetic order down to zero temperature. The model describes a three-dimensional classical spin liquid [10, 12, 20]. In this section, we present a brief review of its properties.

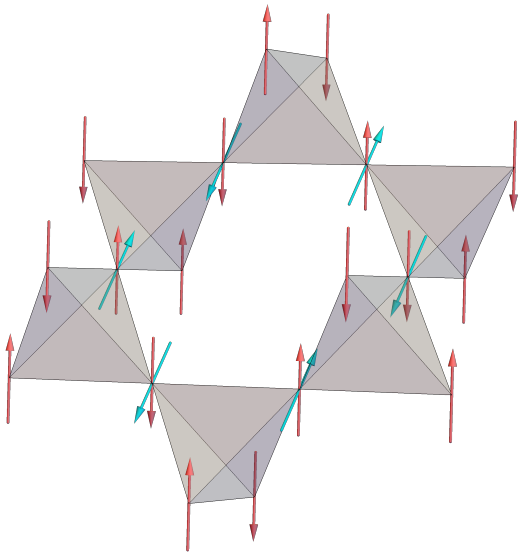

Figure 2.6: A collinear antiferromagnetic state in red arrows and a soft mode in blue arrows on a closed loop.

2.3.1 Zero modes

We start with a collinear antiferromagnetic state with two pairs of anti-aligned spins on each tetrahedron, see Figure 2.6. Without loss of generality, we set all spins along the global z direction. Similar to the Ising case, on each tetrahedra,

$$H_{\boxtimes} = (J_H/2)(\mathbf{s}_0 + \mathbf{s}_1 + \mathbf{s}_2 + \mathbf{s}_3)^2 + \text{const.} \tag{2.8}$$

on every tetrahedron, this spin state obviously minimizes the exchange Hamiltonian.

Consider small deviations from this ground state, i.e. nonvanishing x and y components. As unit vectors, spin states become

$$\mathbf{s}_i = \left(x_i, y_i, \pm\sqrt{1 - x_i^2 - y_i^2}\right). \tag{2.9}$$

Evaluate the exchange Hamiltonian with these spin states, and we get the energy potential for variables x_i and y_i, which governs their dynamics by entering the right-

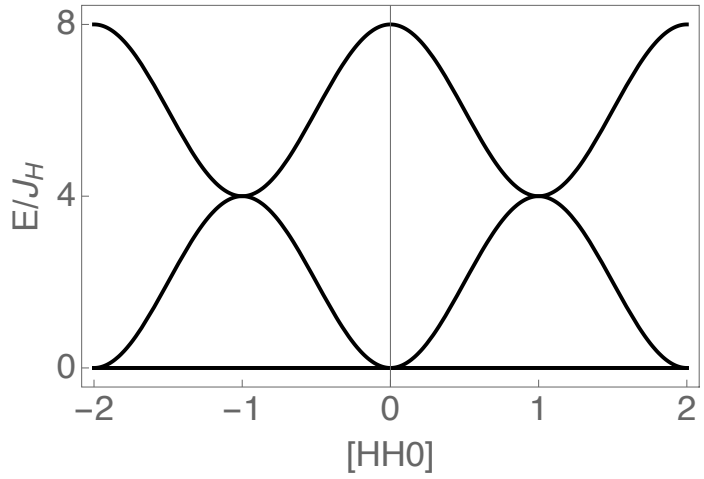

Figure 2.7: Eigenvalues of the interaction matrix for deviations from the collinear antiferromagnetic ground state plotted along a high symmetry direction [HH0] in the momentum space.

hand side of spin precession Equation (1.2). With the potential approximated to quadratic order, the equation is linear. The solutions are dynamical modes called linear spin waves, see Section 3.3.

Since x and y components are equivalent and independent, we focus on only one of them. We look into the property of the potential energy,

$$U(\{x_i\}) = \frac{J_H}{2} \sum_i \left(\sum_{j \in i} x_i x_j + 2x_i^2 \right), \tag{2.10}$$

where j labels nearest neighbors of $\mathbf{r}_i$. The Fourier transform gives the interaction matrix between four sublattices

$$A(\mathbf{q}) = J_H \begin{pmatrix} 2 & c_{yz}^+ & c_{xz}^+ & c_{xy}^+ \\ c_{yz}^+ & 2 & c_{xy}^- & c_{xz}^- \\ c_{xz}^+ & c_{xy}^- & 2 & c_{yz}^- \\ c_{xy}^+ & c_{xz}^- & c_{yz}^- & 2 \end{pmatrix}, \tag{2.11}$$

where $c^{\pm}_{\mu\nu} = 2\cos[\pi(q_\mu \pm q_\nu)/2]$. The eigenvalues are

$$\epsilon_{1,2} = 0, \quad \epsilon_{3,4} = 4 \pm 2\sqrt{1 + \cos\frac{q_y}{2}\cos\frac{q_z}{2} + \cos\frac{q_x}{2}\cos\frac{q_z}{2} + \cos\frac{q_x}{2}\cos\frac{q_y}{2}}. \tag{2.12}$$

A plot of them along $q_x = q_y$ and $q_z = 0$ is given in Figure 2.7.

There are two zero modes at any wavevector $\mathbf{q}$. Deviations (from the ground state we started with) in the form of the eigenvectors of zero modes cost no energy at the harmonic level (to the second order in deviations from equilibrium). They exist at all length scale. For example, in Figure 2.6, we can tilt all spins around the hexagon loop away from the ground state by the same angle, the total exchange energy does not change. We simply change the ground state into a different ground state. We can call the modes mediating the movement inside the ground state manifold tangential modes. Modes with a nonzero energy cost would then be called transverse as they take the system out of the ground-state manifold.

At zero temperature, the motion of the x and y modes are trapped at the bottom of the energy potential. Only the zero modes contribute to the statistical property of the system. From the corresponding eigenvectors $\mathbf{v}_1$ and $\mathbf{v}_2$, we can calculate the the Fourier transform of the spin correlations

$$\langle s^\mu_a(\mathbf{q}) s^\nu_b(-\mathbf{q})\rangle = \delta_{\mu\nu}\sum_m (\mathbf{v}_m)_a (\mathbf{v}_m)_b. \tag{2.13}$$

The static structure factor $\mathcal{S}(\mathbf{q}) = \sum_{\mu\nu}\sum_{ab}\langle s^\mu_a(\mathbf{q}) s^\nu_b(-\mathbf{q})\rangle$ in the a high symmetry plane in the momentum space is plotted in Figure 2.8. No Bragg peaks are present, indicating the absence of long-range magnetic order.

The characteristic features of the static structure factor are the sixfold pinch points ([002], [111], etc.) and the strong angular dependence around them. They can be captured by the long-range statistic of the ground state, in a coarse-grained model.

2.3.2 Long-range correlation

The existence of a large number of zero modes (two per wavevector) is an indication of the high frustration of the system. Actually, there is an entire manifold of ground states of macroscopically high dimensionality. According to the exchange Hamiltonian Equation (2.8), a spin configuration is a ground state as long as it satisfy

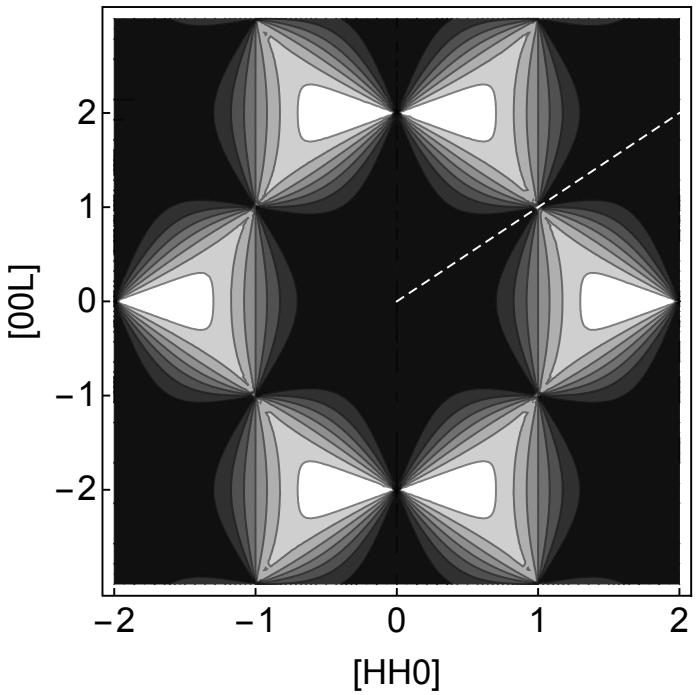

Figure 2.8: Static structure factor of Heisenberg pyrochlore antiferromagnet in the [HHL] plane.

the constraint $\sum_{i\in\boxtimes} \mathbf{s}_i = 0$, that the sum of four spins vanishes, on all tetrahedra. This constraint is similar to the ice rule, but with all three components of the total spin vanishing separately.

Define three vector fields on the pyrochlore lattice $\mathbf{B}^\mu(\mathbf{r}_i) = s_i^\mu \mathbf{z}_i$, where $\mu = x, y, z$ denotes the spin component and $\mathbf{z}_i$ is along the local $\mathbf{z}$ direction at site $\mathbf{r}_i$ defined in Figure 2.4 (a).

We go to a coarse-grained model where $\mathbf{B}^\mu(\mathbf{r})$ are continuous vector fields that vary smoothly in space. The ground state constraint implies the divergence-free condition for the vectors fields $\nabla \cdot \mathbf{B}^\mu(\mathbf{r}) = 0$.

Upon coarse-graining, for most ground states, the value of $\mathbf{B}^\mu(\mathbf{r})$ largely averages out among the disordered spin states. We thus capture this entropic preference for small values of $\mathbf{B}^\mu(\mathbf{r})$ by the partition function [20]

$$\mathcal{Z}[\mathbf{B}^\mu(\mathbf{r})] = \int \mathcal{D}(\mathbf{B}^\mu) \exp\left[-\frac{K}{2}\sum_\mu \int d^3\mathbf{r}\ (\mathbf{B}^\mu)^2\right], \tag{2.14}$$

where K is the isotropic stiffness constant. It describes the long-wavelength fluctuations of the divergence-free fields $\mathbf{B}^\mu(\mathbf{r})$.

To perform the integral with true independent variables of the system, we resolve the constraint by inducing a vector potential $\mathbf{A}^\mu$ with $\mathbf{B}^\mu = \nabla \times \mathbf{A}^\mu$. The Coulomb gauge $\nabla \cdot \mathbf{A} = 0$ has the form $\mathbf{q} \cdot \mathbf{A}^\mu = 0$ in the momentum space. Therefore, $\mathbf{A}^\mu$ only has the two components perpendicular to the wavevector $\mathbf{q}$. The correlation functions between them can be evaluated from the Gaussian form of the partition function in

the momentum space. The correlations between $\mathbf{B}^{\mu}(\mathbf{r})$ fields are

$$\langle (\mathbf{B}^{\mu})_k(\mathbf{q})(\mathbf{B}^{\nu})_\ell(-\mathbf{q})\rangle \propto \delta_{\mu\nu}\left(\delta_{k\ell} - \frac{q_k q_\ell}{q^2}\right). \tag{2.15}$$

The correlations in real space is dipolar,

$$\langle (\mathbf{B}^{\mu})_k(\mathbf{r})(\mathbf{B}^{\nu})_\ell(0)\rangle \propto \delta_{\mu\nu}\frac{3r_k r_\ell - r^2\delta_{k\ell}}{r^5}. \tag{2.16}$$

This is the origin of the angular dependence we observe in the static structure factor, Figure 2.8. At the same time, the correlations do not decay exponentially, as would be expected in a high-temperature disordered (paramagnetic) phase. They fall off as a power law [20, 21], which is characteristic of a critical state intermediate between order and disorder.

2.3.3 Low-energy dynamics

The zero modes govern not only the long-range correlations of the system, but also the low-energy, or long-time-scale, dynamics. They mediate the motion inside the continuously connected ground state manifold, which is very different from the transverse excitations described by spin waves at finite energies. To model the spin dynamics, we integrate out hard spin waves (which represent fast precession close to a ground state) to obtain the slow dynamics along the ground-state manifold. This, of course, cannot be done rigorously since there is no energy gap in the excitations. But in spirit, this can be done, as Moessner and Chalker have shown in References [22,23].

The philosophy of our approach can be expressed in a hydrodynamic model—the Cahn-Hilliard model or model B [24]

$$\frac{\partial \varphi}{\partial t} = \gamma \nabla^2 \frac{\delta H}{\delta \varphi} + \xi, \tag{2.17}$$

It has two important features that make it applicable to a spin system. Firstly, the model respects certain conservation law. Consider the current of field φ driven by the generalized force $\delta H/\delta\varphi$, $\mathbf{j} \propto -\nabla(\delta H/\delta\varphi)$. The equation is like the continuity equation between the density and current. The field φ is conserved. Secondly, fluctuations enter the model in the Gaussian noise ξ.

To construct a spin model, φ can be replaced by spin variables and H by an exchange Hamiltonian, accordingly the spatial differential should be done on a discrete lattice, etc. We leave the details to Section 3.1. Here we simply point out that the model inherits these features: angular momentum is conserved (spins cannot be created or destroyed) and transverse excitations are effectively integrated out, leaving the dynamics relaxational with decay time $\tau^{-1} = \gamma \mathbf{q}^2$.

Since the transverse excitations cost energy, they show up at a finite frequency that is typically much faster than the decay rate of the ground state, especially at long wavelength. From the view of the ground state motion, the spin waves are effectively incoherent and their amplitudes fluctuate randomly, providing a white noise background [23]. In the presence of random "kicks", a state relaxing towards one ground state can be suddenly shifted to a different state and starts to relax to a different ground state. Thus the finite-frequency spin waves are not totally lost in

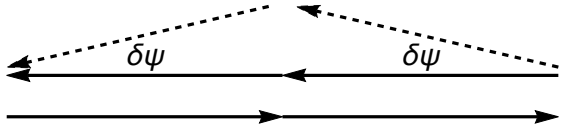

Figure 2.9: A soft mode of excitation on a collinear ground state [23]. Deviations $\delta\psi$ from the ground state create a total spin $\propto (\delta\psi)^2$ hence an energy $\propto (\delta\psi)^4$, vanishing on the harmonic level

this theory. They are essential in driving the motion between the degenerate ground states.

2.3.4 Discussion

The existence of the classical spin liquid phase at zero temperature is established based on the macroscopic degeneracy of the ground states. At finite temperature, however, the free energy also depends on the entropy, which is weighed by the landscape of thermal fluctuations around a ground state. In models such as the Heisenberg kagome antiferromagnet [25] and the XY pyrochlore antiferromagnet [26,27], thermal fluctuations favor a few discrete states out of the continuously degenerate ground state manifold and lead to magnetic order. This phenomenon is called "order-by-disorder" [28–30]. For the antiferromagnetic Heisenberg model on a pyrochlore lattice, thermal fluctuations favor collinear states because of their extra soft modes (in addition to fluctuations within the ground state manifold), as shown in Figure 2.9. But no particular ground states are selected [31], so the system remains a spin liquid. This has been confirmed by Monte Carlo simulations [22, 23].

Quantum effects, admittedly, open a more intriguing territory. While the exoticness of classical spin liquids lies in the capability of the system to explore an extensively degenerate ground state manifold, it is possible for quantum spins to enter a single ground state that is a superposition of all these degenerate states and highly entangled throughout the system [3, 7, 32].

Unfortunately, very little is know about the quantum version of the Heisenberg model on a pyrochlore lattice. The pseudofermion functional renormalization group method finds a quantum spin liquid phase for this model with spin$-1/2$ and spin-1, and shows it is robust against small next-nearest neighbor interactions and breathing anisotropies [33]. The susceptibility calculation also informs us that the physical responses are still mostly governed by the ice rule. Quantum Monte Carlo studies also support the existence of the Coulomb phase for the S=1/2 quantum spin ice in the Heisenberg limit [34, 35]. But the specifics of the ground state and excitations remain unknown.

Chapter 3

Dynamical Models

Positive identification of spin liquids in experiments is challenging because they are—at least initially were—defined primarily by the lack of magnetic order. Theoretical developments of the last two decades have somewhat alleviated this problem: we now know that many types of quantum spin liquids possess topological order of specific types. However, probing topological order experimentally is not an easy task. We thus rely heavily on measurements and understanding of the dynamics of the system. Experimentally, we have been looking for characteristic signatures in the excitation spectrum. Excitations in quantum spin liquids can be quite unusual, including fractionalized [36, 37] quasiparticles such as spinons (electric charges) in the U(1) spin liquid [16, 38, 39], and Majorana fermions in the Kitaev honeycomb model [40–42]. The idea is to identify specific signatures of these unusual excitations in experimental data and to devise a theoretical framework for understanding the

underlying behavior.

As we have seen in the last two chapters, standard models reveal the precessional and relaxational dynamics of spin systems. Now we apply these methods to a Hamiltonian that describes a real material, study its dynamics and compare the theoretical models with experimental observations. In this chapter, we discuss dynamical models with a more general interaction Hamiltonian—Heisenberg pyrochlore antiferromagnet plus small perturbations.

Small perturbations, such as anisotropic interactions (off-diagonal terms in the nearest-neighbor interaction matrix (2.4)) and further-neighbor interactions, are likely to be present in a material realization of the model. On one hand, perturbation terms can lift the degeneracy of the ground state manifold and induce magnetic orders. Earlier research has found that anisotropic nearest-neighbor perturbations lead to antiferromagnetic long-range orders with a tetrahedron as the unit cell [13, 43], and Heisenberg next-nearest-neighbor interactions gives more complicated spiral states [33,44]. It is still a question whether a single classical long-range ordered ground state is selected in the presence of both. On the other hand, when the perturbations are weak and the temperature is finite (but not necessarily higher than the energy scale of the perturbations), the perturbed model could remain paramagnetic and enter an approximate spin liquid state, because of the strong frustration.

Going to even lower temperature, the classical model is expected to eventually develop an order, or freeze into a disordered configuration. But when the spins are

small ($S = 1/2$ or 1), quantum fluctuations become important. Similar to the effect of thermal fluctuations, quantum fluctuations may prefer an ordered state, through the mechanism known as quantum "order by disorder" [30, 45, 46]. Or they may lead to an exotic quantum spin liquid state that cannot be described by any classical order. The fate of the system is again mysterious.

This is the situation we find ourselves in. In this chapter, we present three complementary theoretical methods for the perturbed Heisenberg pyrochlore antiferromagnet at low temperatures and in the paramagnetic phase. We also aim to clarify the essence of each method, and how they are related to each other. The combination of these methods allows us to piece together a physical picture for the spin dynamics of realistic pyrochlore antiferromagnets exemplified by $NaCaNi_2F_7$.

These methods are adapted from References [47–51] and some have been developed in collaboration with Hitesh J. Changlani, Kemp W. Plumb, Oleg Tchernyshyov, and Roderich Moessner [52].

3.1 Stochastic large-n model

The term "large-n" refers to the spherical $O(n)$ model for a spin with $n \to \infty$ components [53]. In this model, we self-consistently fix the length of spins and the spherical approximation makes the condition easier to work with—it is in a Gaussian form. Therefore this model is also called self-consistent Gaussian approximation

(SCGA) [54].

As we pointed out in Section 2.3.3, the stochastic model describes the low-energy motion within or near the ground state manifold. We consider the spin configuration drifts under a generalized force, while white a noise with Gaussian distribution represents thermal fluctuations [47]:

$$\frac{d}{dt}s_i^\mu = \gamma \sum_j \Delta_{ij} \frac{\partial E}{\partial s_j^\mu} + \xi_i^\mu(t), \tag{3.1}$$

where γ is a dynamical parameter like a diffusion constant. $\Delta_{ij} = A_{ij} - z\delta_{ij}$ is the lattice laplacian, where A_{ij} takes value 1 for nearest neighbors and 0 for others, and z is the coordination number.

We soften the physical spins, only fixing the global spin with $n = 3N$, or the average length of each spin component,

$$NS^2 = \sum_i \sum_\mu \langle (s_i^\mu)^2 \rangle. \tag{3.2}$$

Generating generalized forces on spins is the weight in the Boltzmann distribution

$$\beta E \equiv \sum_{ij} \sum_{\mu\nu} \frac{1}{2} (\beta J_{ij}^{\mu\nu} + \lambda \delta_{ij} \delta^{\mu\nu}) s_i^\mu s_j^\nu, \tag{3.3}$$

where $\beta = 1/k_B T$ and λ is the Lagrange multiplier enforcing a fixed spin length. Its value is solved self-consistently as follows.

We perform the lattice Fourier transform on each fcc sublattice a,

$$\tilde{s}_a^\mu(\mathbf{q}) = \frac{1}{\sqrt{N_c}} \sum_{i \in a} e^{-i\mathbf{q}\cdot\mathbf{r}_i} s_i^\mu, \tag{3.4}$$

where N_c is the number of up- or down- tetrahedra, $N_c = N/4$. The lattice Laplacian Δ_{ij} and the interaction matrix $J_{ij}^{\mu\nu}$ transform accordingly into the momentum space, becoming $\Delta(\mathbf{q})$ and $J(\mathbf{q})$ respectively. The four sublattices and three spin components make $\{\tilde{s}_a^\mu(\mathbf{q})\}$ 12 variable. We define two 12×12 matrices

$$P = -\Delta(\mathbf{q}) \otimes I_3 \quad \text{and} \quad Q = J(\mathbf{q}) + (\frac{\lambda}{\beta})I_{12}, \tag{3.5}$$

where I_3 is the 3×3 identity matrix and $\otimes$ is the direct product operation.

The condition 3.2 can then be expressed as an equation for λ,

$$NS^2 = \sum_{\mathbf{q}} \sum_{\rho} \frac{1}{\beta\epsilon_\rho(\mathbf{q}) + \lambda} = \sum_{\mathbf{q}} \mathrm{Tr}(Q^{-1}), \tag{3.6}$$

where $\epsilon_\rho(\mathbf{q})$ is the eigenvalues of $J(\mathbf{q})$, and $\mathbf{q}$ is summed over the first Brillouin zone of the fcc lattice.

The noise variables follow the independent Gaussian distribution

$$\begin{aligned} &\langle \xi_i^\mu(t) \rangle = 0, \\ &\langle \xi_i^\mu(t) \xi_j^\nu(t') \rangle = -\frac{2\gamma}{\beta} \Delta_{ij} \delta^{\mu\nu} \delta(t - t'), \end{aligned} \tag{3.7}$$

where the amplitude of the correlation is determined by the fluctuation-dissipation theorem, see Section 3.1.2.

3.1.1 Structure factors

There are several forms of the structure factor. Inelastic neutron scattering directly measures the dynamical structure factor, which is of our primary interest. It

is the Fourier transform of the spin correlation function into energy/frequency and momentum/wavevector space:

$$\mathcal{S}^{\mu\nu}(\mathbf{q},\omega) = \frac{1}{2\pi N}\sum_{i,j=1}^{N}\int_{-\infty}^{\infty} dt\, e^{-i\mathbf{q}\cdot(\mathbf{r}_i-\mathbf{r}_j)+i\omega t}\langle s_i^{\mu}(t)s_j^{\nu}(0)\rangle. \tag{3.8}$$

It can be derived analytically from the stochastic model.

The Fourier transform takes the equation of motion (3.1) to an algebraic equation for the 12-component vector $\tilde{S}(\mathbf{q},\omega) = (\tilde{s}_0^x, \tilde{s}_0^y, \tilde{s}_0^z, \ldots, \tilde{s}_3^x, \tilde{s}_3^y, \tilde{s}_3^z)^T$

$$\tilde{S}(\mathbf{q},\omega) = G(\mathbf{q},\omega)\,\tilde{\xi}(\mathbf{q},\omega), \tag{3.9}$$

where the Green's function is

$$G^{-1}(\mathbf{q},\omega) = -i\omega I_{12} + \gamma PQ, \tag{3.10}$$

and $\xi(\mathbf{q},\omega)$ is the Fourier transform of the white noise.

Because P and Q are real and symmetric, Q is positive definite and P is semi-positive definite, there exists a similarity transformation under matrix V to obtain a diagonal matrix Λ with real and non-negative entries (generally $PQ \neq QP$),

$$QP = V\Lambda V^{-1}. \tag{3.11}$$

Substituting in the correlation function of the Gaussian noise (3.7),

$$\begin{aligned}\langle \tilde{S}_\rho(\mathbf{q},\omega)\tilde{S}_\sigma(-\mathbf{q},-\omega)\rangle &= \frac{2\gamma}{\beta}(GPG^\dagger)_{\rho\sigma} \\ &= \frac{2\gamma}{\beta}\left[PV(\omega^2+\gamma^2\Lambda^2)^{-1}V^{-1}\right]_{\rho\sigma}.\end{aligned} \tag{3.12}$$

The dynamical structure factor (3.8) thus evaluates to be

$$\mathcal{S}^{\mu\nu}(\mathbf{q},\omega) = \frac{1}{8\pi}\sum_{\rho\sigma}\kappa_\rho^\mu\kappa_\sigma^\nu\langle\tilde{S}_\rho(\mathbf{q},\omega)\tilde{S}_\sigma(-\mathbf{q},-\omega)\rangle, \tag{3.13}$$

where $\kappa^\mu = (1,1,1,1)\otimes\mathbf{e}^\mu$, $\mathbf{e}^\mu = \mathbf{x},\mathbf{y},\mathbf{z}$. In Figure 3.1, we plot the result in a high symmetry plane in the momentum space for the nearest-neighbor Heisenberg interaction we discussed in last chapter. As the energy goes higher, the intensity decays in a Lorentzian form (3.12), indicating diffusive spin dynamics.

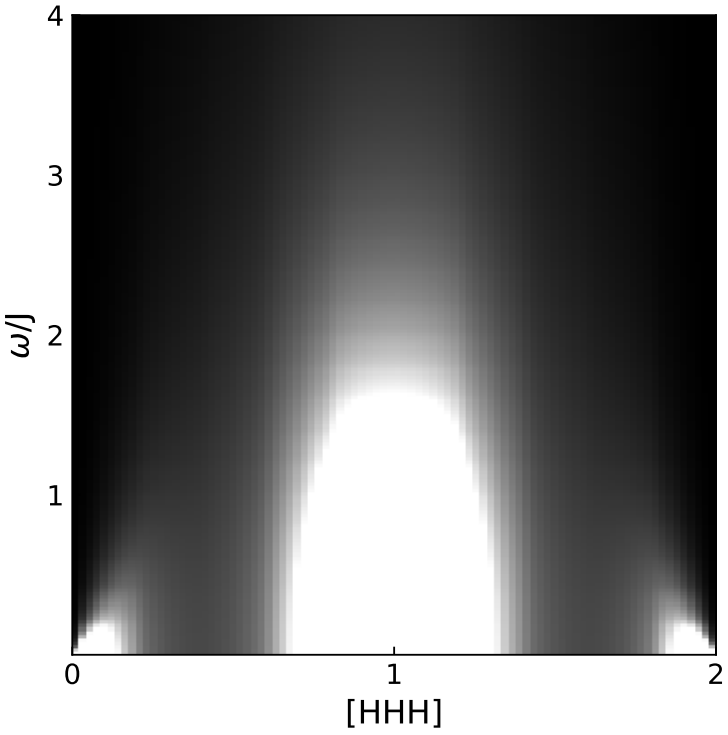

Figure 3.1: Spin diffusion in the Heisenberg pyrochlore antiferromagnet. The dynamical structure factor at $T = 0.05J_H$ is plotted in the energy-momentum space for a cut along [HHH] as shown in Fig, 2.8.

The Lorentzian distribution transforms to exponential decay in time,

$$\int\frac{d\omega}{2\pi}\frac{e^{-i\omega t}}{\omega^2+\gamma^2\Lambda_\alpha^2} = \frac{e^{-\gamma\Lambda_\alpha t}}{2\gamma\Lambda_\alpha}. \tag{3.14}$$

The static structure factor, also called instantaneous structure factor, can be derived as

$$\langle \tilde{s}_\rho(\mathbf{q})\tilde{s}_\sigma(-\mathbf{q})\rangle_{t=0} = \int \frac{d\omega}{2\pi}\langle \tilde{s}_\rho(\mathbf{q},\omega)\tilde{s}_\sigma(-\mathbf{q},-\omega)\rangle = \frac{1}{\beta}(Q^{-1})_{\rho\sigma}, \tag{3.15}$$

where the matrix Q is defined in Equation (3.5).

This is also how the static structure factor is calculated from inelastic neutron scattering data, by integrating the dynamical structure factor over energy up to the highest energy with appreciable intensities.

Theoretically, the same result can come directly from the Gaussian statistics of the spin variables (3.3). In spite of the approximation, the result can quite exactly describe the instantaneous correlation in the system, especially when we are working at a temperature that is low yet not low enough for the magnetic order to develop. Since the classical model tends to order at a sufficiently low temperature, our method breaks down at a theoretical "critical temperature", below which it is no longer applicable. This hypothetical critical temperature $k_B T_c = \beta_c$ can be determined by a finite size scaling effect. We refer to Appendix B for details.

The static structure calculated in this way can be directly compared with Monte Carlo simulations, see Section 4.2.

Also, the correlation works well for all length scales. The static structure factor (3.15) peaks at some wavevectors $\mathbf{q}$, reflecting the tendency of the system to order at those wavevectors, where the excitations are likely to condense first. This indicates stronger short-range correlations are developing upon cooling, although no

long-range magnetic orders are guaranteed to form. Thus, the model tells us more than the long-range hydrodynamical features it targets at.

In general, at a time $t \neq 0$, we have the time-dependent dynamical structure factor

$$\mathcal{S}^{\mu\nu}(\mathbf{q}, t) = \int \frac{d\omega}{2\pi} e^{-i\omega t} \mathcal{S}^{\mu\nu}(\mathbf{q}, \omega). \tag{3.16}$$

This result can be compared with molecular dynamics simulations at long time scales to determine the dynamical parameter γ, for example, see Figure 3.2.

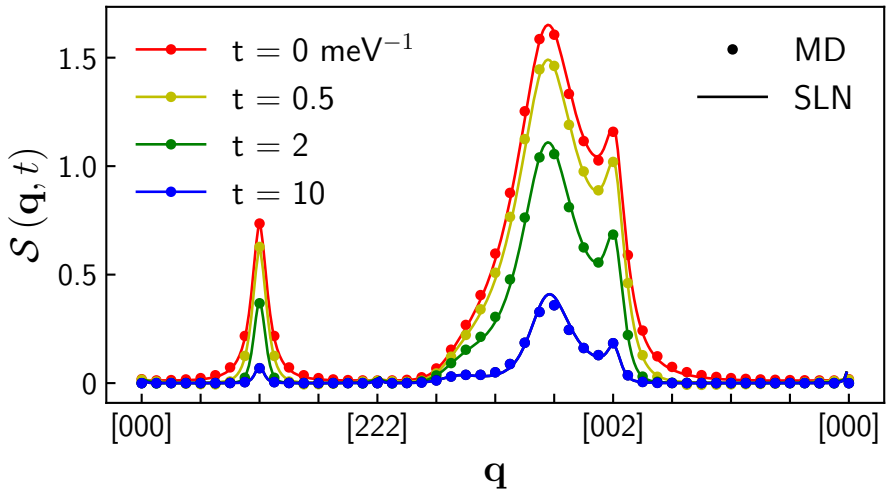

Figure 3.2: The time-dependent dynamical structure factor from the molecular dynamics (dots) and stochastic model (lines) along a momentum path. The calculation is done for $NaCaNi_2F_7$ to fit the dynamical parameter γ in the stochastic model, where $\gamma = 0.165$.

3.1.2 Fluctuation-dissipation theorem

The fluctuation dissipation theorem relates the correlation function of a physical variable to the imaginary part of the response function of the same variable. The

former quantifies thermal fluctuations, and the latter is proportional to the rate at which energy is dissipated as heat. The classical fluctuation-dissipation theorem requires for spin variables

$$\begin{aligned} \mathrm{Im}\chi_{\rho\sigma}(\mathbf{q},\omega) &= \frac{1}{2}\beta\omega\langle\tilde{S}_\rho(\mathbf{q},\omega)\tilde{S}_\sigma(-\mathbf{q},-\omega)\rangle \\ &= \frac{1}{2}\beta\omega\sum_{\rho'\sigma'} G_{\rho\rho'}\langle\tilde{\xi}_{\rho'}(\mathbf{q},\omega)\tilde{\xi}_{\sigma'}(-\mathbf{q},-\omega)\rangle G^\dagger_{\sigma'\sigma}, \end{aligned} \tag{3.17}$$

and it relates the linear response of spins to a magnetic field in the stochastic model (3.1),

$$\mathrm{Im}\chi_{\rho\sigma} = \gamma\left[(\mathrm{Im}G)P\right]_{\rho\sigma}. \tag{3.18}$$

Comparing the two we can conclude that the exact form of white noise correlations (3.7) is required.

3.1.3 Fokker-Planck equation

In this section, we derive the Fokker-Planck equation for our stochastic model (3.1) on a discrete lattice, following the Kramers-Moyal expansion [51].

Given an initial spin configuration $\{(s^\rho_\ell)_0\}$ at t_0, we consider the conditional probability distribution

$$p(\{s^\rho_\ell\}, t \,|\, \{(s^\rho_\ell)_0\}, t_0) = \Big\langle \prod_{\ell,\rho} \delta\left[s^\rho_\ell - s^\rho_\ell(t)\right] \Big\rangle_{\{(s^\rho_\ell)_0\},t_0}. \tag{3.19}$$

The stochastic equation (3.1) gives the configuration after evolving $s^\mu_i(t)$ by δt,

$$s^\mu_i(t+\delta t) = s^\mu_i(t) + \gamma\delta t\sum_j \Delta_{ij}\frac{\partial E}{\partial s^\mu_j(t)} + \int_t^{t+\delta t} dt'\xi^\mu_i(t'). \tag{3.20}$$

Up to first order in δt, we expand

$$\begin{aligned}&\left\langle \prod_{\ell,\rho} \delta\left[s_\ell^\rho - s_\ell^\rho(t+\delta t)\right] \right\rangle_{\{s_\ell^\rho(t)\},t} \\ &\quad = \left[1 - \gamma\delta t \sum_{ij,\mu} \Delta_{ij} \frac{\partial E}{\partial s_j^\mu(t)} \frac{\partial}{\partial s_i^\mu} - \frac{\gamma}{\beta}\delta t \sum_{ij,\mu} \Delta_{ij} \frac{\partial}{\partial s_i^\mu}\frac{\partial}{\partial s_j^\mu}\right] \prod_{\ell,\rho} \delta\left[s_\ell^\rho - s_\ell^\rho(t)\right],\end{aligned} \tag{3.21}$$

where we have used

$$\int_t^{t+\delta t} dt_1 \int_t^{t+\delta t} dt_2 \langle \xi_i^\mu(t_1)\xi_j^\nu(t_2)\rangle = -\frac{2\gamma}{\beta}\delta t \Delta_{ij}\delta^{\mu\nu}. \tag{3.22}$$

We now have the Fokker-Planck equation for the Cahn-Hilliard model on a discrete lattice of spins in the paramagnetic phase

$$\frac{\partial p}{\partial t} = -\gamma \sum_{ij}\sum_{\mu} \Delta_{ij} \frac{\partial}{\partial s_i^\mu}\left[\left(\frac{\partial E}{\partial s_j^\mu} + \frac{1}{\beta}\frac{\partial}{\partial s_j^\mu}\right) p\right]. \tag{3.23}$$

The probability distribution stops evolving when

$$p = p_{\text{eq}} = \frac{1}{Z}\exp(-\beta E), \tag{3.24}$$

where Z is the partition fucntion.

The results can be easily generalized to study the relaxation of nematic or phononic systems. For a general continuum formalism and its applications, see References [55, 56].

We can also generalize these equations from classical to quantum, non-commuting variables. In the semi-classical viewpoint, we should consider the Poisson brackets between spin operators.

3.2 Molecular Dynamics

The full dynamics of interacting classical spins can be simulated by integrating the Landau-Lifshitz equation (1.2), which describes the precessional motion of spins.

Following References [22, 23, 47], an initial configuration (IC) of spins can be obtained by a Monte Carlo (MC) run from the Boltzmann distribution $\exp(-\beta H)$ at finite temperature; and then evolved deterministically.

The averaged time-dependent spin correlation functions in real space are

$$\langle s_i^\mu(t) s_j^\nu(0)\rangle = \frac{1}{N_s} \sum_{\text{IC from MC}} s_i^\mu(t) s_j^\nu(0)\big|_{\text{IC}}, \tag{3.25}$$

where N_s is the number of MC samples. Averaging over many initial configuration samples is necessary because the precessional model preserves the total energy of the system. The spin configuration evolves along an equipotential surface, exploring only a very limited part of the classical phase space.

To compute dynamical structure factor, we perform the discrete Fourier transform with T_s time steps in total,

$$\tilde{s}^\mu(\mathbf{q},\omega) = \frac{1}{\sqrt{N}} \sum_i \frac{1}{T_s} \sum_t e^{-i\mathbf{q}\cdot\mathbf{r}_j + i\omega t} s^\mu(\mathbf{r}_i, t). \tag{3.26}$$

Then

$$\mathcal{S}^{\mu\nu}(\mathbf{q},\omega) = \frac{T_s}{2\pi} \langle \tilde{s}^\mu(\mathbf{q},\omega) \tilde{s}^\nu(-\mathbf{q},-\omega)\rangle, \tag{3.27}$$

For an adequately fine time resolution and long evolution time, the integration $\int_0^\infty (d\omega/\pi)\, \mathcal{S}^{\mu\nu}(\mathbf{q},\omega)$ should be roughly equal to the static spin correlations $\mathcal{S}^{\mu\nu}(\mathbf{q})$ of the initial spin configuration.

3.3 Linear spin wave theory

For a disordered state, the dispersion is not well-defined any more, but the precessional dynamics persists as long as there are transverse fluctuations, and can be profiled in the dynamical spin correlations [1, 54, 57].

A typical application of linear spin wave theory begins with the determination of a classical ground state. The simplest ground states have a small unit cell, such as a single tetrahedron in the pyrochlore lattice, which repeats periodically in space, so spin waves have a well-defined wavenumber. The Hamiltonian in momentum space is in a block diagonal form with no interaction between different wavecectors $\mathbf{q}$. There are only a few eigenmodes, which have sharp dispersions. However, the situation is markedly different for ground states that lack magnetic order or have very large unit cells.

This latter situation is typical for the classical Heisenberg model on the pyrochlore lattice. It has an enormous number of ground states which satisfy the condition $\sum_{i\in\boxtimes} \mathbf{s}_i = 0$, and most of them are inhomogeneous. (Small anisotropic and further-neighbor interactions lift this degeneracy, but can still allow many low-energy minima.) For a large but finite lattice, we can use a Monte Carlo run or simulated annealing to generate a random ground state and then perform linear spin wave theory in real space directly using the formalism given in the following sections. Previous work on this can be found in Reference [57, 58].

In this section, we discuss linear spin wave theory from both classical and quantum

perspectives.

3.3.1 Classical approach

We begin with a classical ground state (or generally a local minimum of energy), so that every spin $\mathbf{s}_i$ is in a state of equilibrium. It is convenient to define a local frame with three mutually orthogonal unit vectors $\mathbf{u}_i$, $\mathbf{v}_i$, and $\mathbf{w}_i$, where $\mathbf{u}_i = \mathbf{s}_i/S$ points along the equilibrium direction. Small deviations of $\mathbf{s}_i$ from its equilibrium position can be parametrized in terms of two coordinates x_i and y_i as follows:

$$\begin{aligned} \mathbf{s}_i &= \sqrt{S^2 - S(x_i^2 + y_i^2)}\,\mathbf{u}_i + \sqrt{S}(x_i\mathbf{v}_i + y_i\mathbf{w}_i) \\ &\approx \left(S - \frac{x_i^2 + y_i^2}{2}\right)\mathbf{u}_i + \sqrt{S}(x_i\mathbf{v}_i + y_i\mathbf{w}_i). \end{aligned} \tag{3.28}$$

The dynamics of variables x_i and y_i is governed by the Lagrangian

$$L = \sum_i \frac{1}{2}\left(y_i\frac{dx_i}{dt} - x_i\frac{dy_i}{dt}\right) - U, \tag{3.29}$$

where U is the potential energy for x_i and y_i from plugging the spin expression into the Hamiltonian. The kinetic term expresses the Berry phase in the spin action to the lowest order in transverse fluctuations x and y. Upon expanding it to the second order in the deviations from equilibrium, we obtain

$$L = \frac{1}{2}z^T\Gamma\frac{d}{dt}z - \frac{1}{2}z^T\mathcal{H}z, \tag{3.30}$$

where $\mathcal{H}$ is a symmetric matrix, Γ is a skew-symmetric matrix and z is a column

vector:

$$z \equiv \begin{pmatrix} x_1 \\ y_1 \\ \vdots \\ x_N \\ y_N \end{pmatrix}, \quad \Gamma = \begin{pmatrix} 0 & -1 & \dots & 0 & 0 \\ 1 & 0 & \dots & 0 & 0 \\ \vdots & \vdots & \ddots & \vdots & \vdots \\ 0 & 0 & \dots & 0 & -1 \\ 0 & 0 & \dots & 1 & 0 \end{pmatrix}. \tag{3.31}$$

Classical equations of motion for the deviations z are obtained from the Lagrangian (3.30),

$$\Gamma \frac{d}{dt} z = \mathcal{H} z. \tag{3.32}$$

An oscillatory Ansatz

$$z(t) = \sum_\alpha c_\alpha \psi_\alpha e^{-i\omega_\alpha t}, \tag{3.33}$$

where c_α is the amplitude, reduces this problem to an algebraic equation for normal modes ψ_α,

$$(i\omega_\alpha \Gamma + \mathcal{H})\psi_\alpha = 0. \tag{3.34}$$

Its solutions have the following properties: the eigenvalues come in pairs of real numbers $\omega_{-\alpha} = -\omega_\alpha$; twin eigenvectors satisfy the relation $\psi^\dagger_{-\alpha}\Gamma\psi_{-\alpha} = -\psi^\dagger_\alpha \Gamma \psi_\alpha$; we thus choose the orthonormalization

$$\psi^\dagger_\beta(-i\Gamma)\psi_\alpha = \mathrm{sgn}(\omega_\alpha)\delta_{\alpha\beta}. \tag{3.35}$$

As a result,

$$\psi^\dagger_\beta \mathcal{H} \psi_\alpha = \mathrm{sgn}(\omega_\alpha)\omega_\alpha \delta_{\alpha\beta} = |\omega_\alpha|\delta_{\alpha\beta}. \tag{3.36}$$

and the potential energy is diagonalized in c_α

$$U = \frac{1}{2}\sum_\alpha \omega_\alpha c_\alpha^* c_\alpha. \tag{3.37}$$

The Boltzmann distribution gives the thermal average of the amplitudes $\langle c_\beta^* c_\alpha\rangle = \delta_{\alpha\beta}/\beta|\omega_\alpha|$, thus

$$\langle z_k(t) z_l(0)\rangle = \sum_\alpha \frac{[\psi_\alpha]_k\,[\psi_\alpha^\dagger]_l}{\beta|\omega_\alpha|} e^{-i\omega_\alpha t}, \tag{3.38}$$

where $k,\, l = 1,\ldots,2N$. Denote $\psi_\alpha^i \equiv ([\psi_\alpha]_{2i}, [\psi_\alpha]_{2i+1})^T$ and $\eta_i^\mu \equiv (v_i^\mu, w_i^\mu)$, The spin correlation functions (3.8) can be expressed as

$$\mathcal{S}^{\mu\nu}_{\rm classical}(\mathbf{q},\omega) = \frac{S}{N}\sum_{i,j=1}^{N} e^{-i\mathbf{q}\cdot(\mathbf{r}_i-\mathbf{r}_j)} \sum_\alpha \frac{(\eta_i^\mu\cdot\psi_\alpha^i)\,(\eta_j^\mu\cdot\psi_\alpha^j)^*}{\beta|\omega_\alpha|}\delta(\omega-\omega_\alpha). \tag{3.39}$$

3.3.2 Quantum statistics

In the quantum approach, the dynamical structure factor can be computed as the imaginary part of the retarded response function

$$\mathcal{G}_+^{\mu\nu} = \frac{1}{\pi N}\sum_{i,j=1}^{N}\int_0^\infty dt\, e^{-i\mathbf{q}\cdot(\mathbf{r}_i-\mathbf{r}_j)+i\omega t}(-i)\langle[s_i^\mu(t), s_j^\nu(0)]\rangle. \tag{3.40}$$

In the low temperature limit, $\beta\omega \gg 0$

$$\mathcal{S}^{\mu\nu}_{\rm quantum}(\mathbf{q},\omega) = \lim_{T\to 0}(1-e^{-\beta\omega})^{-1}{\rm Im}\mathcal{G}_+^{\mu\nu} = {\rm Im}\mathcal{G}_+^{\mu\nu}. \tag{3.41}$$

To evaluate the functional average over the ensemble, we take $t \to -i\tau$ in (3.30) to get the imaginary-time partition function

$$\mathcal{Z} = \int \mathcal{D}z\, \exp\left[-\frac{1}{2}\int_0^\beta d\tau\; z^T(-i\Gamma\frac{d}{d\tau} + \mathcal{H})z\right]. \tag{3.42}$$

In the representation of Matsubara frequencies $\omega_n = 2\pi n/\beta$ ($n \in \mathbb{Z}$),

$$z(\tau) = \frac{1}{\sqrt{\beta}} \sum_{\omega_n} \zeta_n e^{-i\omega_n \tau}. \tag{3.43}$$

We diagonalize the action in the partition function (3.42) by decomposing ζ_n into orthonormal vectors ψ_α (3.35) and calculate the matrix elements of the propagator:

$$\langle \zeta_n \zeta_n^\dagger \rangle_{kl} = \sum_\alpha \frac{[\psi_\alpha]_k \, [\psi_\alpha^\dagger]_l}{-i\omega_n + \omega_\alpha} \mathrm{sgn}(\omega_\alpha). \tag{3.44}$$

Replacing $i\omega_n$ by $\omega + i0^+$ gives the retarded response function

$$\langle z_k(\omega) z_l(-\omega) \rangle_+ = -\sum_\alpha \frac{[\psi_\alpha]_k \, [\psi_\alpha^\dagger]_l}{\omega - \omega_\alpha + i0^+} \mathrm{sgn}(\omega_\alpha). \tag{3.45}$$

The spin correlation function (3.41) is thus

$$\mathcal{S}^{\mu\nu}_{\text{quantum}}(\mathbf{q}, \omega) = \frac{S}{N} \sum_{i,j=1}^{N} e^{-i\mathbf{q}\cdot(\mathbf{r}_i - \mathbf{r}_j)} \sum_\alpha (\eta_i^\mu . \psi_\alpha^i) \, (\eta_j^\mu . \psi_\alpha^j)^* \, \delta(\omega - \omega_\alpha) \mathrm{sgn}(\omega_\alpha), \tag{3.46}$$

with the same notation as in (3.39).

Comparing Equations (3.39) and (3.46), we arrive at a relation between the finite temperature classical calculation and the zero temperature quantum calculation for spin correlations under the linear spin wave framework,

$$\beta\omega \mathcal{S}^{\mu\nu}_{\text{classical}}(\mathbf{q}, \omega) = \mathcal{S}^{\mu\nu}_{\text{quantum}}(\mathbf{q}, \omega), \tag{3.47}$$

which is applicable at low temperature and positive energy transfer ($\beta\omega \gg 1$).

3.3.3 Real space and momentum space calculation

For a ground state with translational symmetry, the potential energy U can be block diagonalized in momentum space. The Fourier transformation is done on each

sublattice,

$$\tilde{s}_a^\mu(\mathbf{q}) = \frac{1}{\sqrt{N_c}} \sum_{i \in a} e^{-i\mathbf{q}\cdot r_i} s_i^\mu. \tag{3.48}$$

For convenience, we rearrange the $2N$-vector z to group the variables of the same unit cell,

$$\begin{aligned} z' &= Rz \\ &= (x_{1,0}, \ldots, x_{1,N_s-1}, y_{1,0}, \ldots, y_{1,N_s-1}, \ldots, x_{N_c,0}, \ldots, x_{N_c,N_s-1}, y_{N_c,0}, \ldots y_{N_c,N_s-1})^T \end{aligned} \tag{3.49}$$

where N_s is the number of sublattices, $N_s N_c = N$, and R is an elementary matrix. Thus the Fourier transformation acts on z as a matrix with blocks

$$W_{ll'} = \frac{1}{\sqrt{N_c}} I_2 \otimes \begin{pmatrix} e^{-i\mathbf{q}_l \cdot \mathbf{r}_{l',0}} & & \\ & \ddots & \\ & & e^{-i\mathbf{q}_l \cdot \mathbf{r}_{l',3}} \end{pmatrix}, \tag{3.50}$$

and

$$\tilde{\mathcal{H}} = W \mathcal{R} \mathcal{H} R^{-1} W^\dagger. \tag{3.51}$$

We end up with the same generalized eigenproblem in each block

$$(i\omega_{l,\alpha'} \tilde{\Gamma} + \tilde{\mathcal{H}}_l) \tilde{\psi}_{l,\alpha'} = 0, \tag{3.52}$$

where $l = 1, \ldots, N_c$ and $\alpha' = 0, \ldots, 2N_s - 1$, and

$$\tilde{\Gamma} = \begin{pmatrix} & -I_{N_s} \\ I_{N_s} & \end{pmatrix}, \qquad W_{ll} \tilde{\Gamma} W_{ll}^\dagger = \tilde{\Gamma}. \tag{3.53}$$

There are $2N$ eigenvectors $\tilde{\psi}$. Each is a $2N_s$-vector in the form of

$$\left[\tilde{\psi}_{\alpha'}(\mathbf{q})\right]_p = \left[\tilde{\psi}_{\alpha=(l,\alpha')}(\mathbf{q})\right]_p = \frac{1}{\sqrt{N_c}} \sum_{l'=0}^{N_s-1} e^{-i\mathbf{q}\cdot\mathbf{r}_{l',p}} (R\psi_\alpha)_{N_s\times l'+p} \tag{3.54}$$

where $\mathbf{r}_{l',a+N_s} = \mathbf{r}_{l',a}$. This keeps the consistency of the normalization of both sets of eigenvectors. In the expression for the dynamical structure factor in real space, absorbing the Fourier transform into the eigenvectors

$$\mathcal{S}^{\mu\nu}_{\text{quantum}}(\mathbf{q},\omega) = \frac{S}{N_s} \sum_{a',b'=1}^{2N_s} \tilde{\eta}^\mu_{a'} \tilde{\eta}^\nu_{b'} \sum_{\alpha'} \left[\tilde{\psi}_{\alpha'}(\mathbf{q})\right]_{a'} \left[\tilde{\psi}^\dagger_{\alpha'}(\mathbf{q})\right]_{b'} \delta(\omega - \omega_{\alpha'}(\mathbf{q})) \operatorname{sgn}(\omega_{\alpha'}) \tag{3.55}$$

where $\tilde{\eta} = (v^\mu_1, \ldots, v^\mu_{N_s}, w^\mu_1, \ldots, w^\mu_{N_s})$. The summation is done for all sublattices hence the $1/N_s$ factor in front. This is consistent with the result in Reference [49].

For a uniform ground state, we expect to see sharp dispersions, while the broadening on the order of J indicates an inhomogeneous ground state.

3.4 Discussion

We now summarize the individual features of the three methods and point out the relations between them. This will be important later, when we compare our theoretical models with experimental results.

The stochastic model of Section 3.1 captures the slow relaxational dynamics of classical spins at low-energy, long-time scale. It represents the spin diffusion driven by thermal fluctuations and reflects the spin dynamics with the lowest energies.

Molecular dynamics cover both the short-time and long-time motion of a classical spin system. It describes the spin precession under local exchange field. For temperatures higher or comparable with the energy barriers between energy minima, it is possible for the system to explore the landscape around many different ground states during the evolution. It also contains information about anharmonic excitations and interactions between spin wave modes, in the form of relaxation of the spin configuration. The long-time limit results are more likely to be consistent with the the stochastic model, when all or most of the ground states are accessible by the initial configuration.

The linear spin wave theory describes harmonic excitations (small-amplitude spin waves) of finite frequency in the vicinity of a specific ground state. The zero modes, connecting degenerate ground states, are not considered. The structure factors from the classical spin wave method can be compared with molecular dynamics at finite frequencies.

For classical spins, excitations are excited through thermal fluctuations. At low temperature, the intensity of dynamical correlations is suppressed according to the Boltzmann factor. Yet similar spin waves from quantum fluctuations have nonvanishing contributions to the dynamical correlations. This is taken into account by the quantum-classical correspondence relation (3.47). Thus, the result from classical molecular dynamics simulations at finite temperature, after a rescaling by $\beta\omega$, can be compared with the quantum linear spin wave theory at zero temperature.

Finally, we emphasize that none of our theoretical approaches relies on the existence of long-range orders or coherent excitations.

Chapter 4

Spin dynamics of $NaCaNi_2F_7$

We now turn to the application of theoretical modelings to understand the spin dynamics in a real and interesting magnetic material—a three-dimensional quantum spin liquid candidate $NaCaNi_2F_7$.

Firstly, the pyrochlore compound $NaCaNi_2F_7$ is an almost ideal realization of the spin-1 antiferromagnetic Heisenberg model on a pyrochlore lattice. It is well described by a weakly perturbed nearest-neighbour Heisenberg Hamiltonian [59].

It has been extremely challenging to synthesize materials that realize the pyrochlore Heisenberg model. The closest realizations of a Heisenberg antiferromagnet on a pyrochlore lattice are found in the cubic spinels [60–65]. Many of these materials exhibit significant exchange interactions extending to the second and third nearest neighbours, which suppress pinch points (features in long-range correlations discussed in Section 2.3) and favors cluster states of spins [48]. Often, magneto-structural tran-

sitions [66] lead to broken-symmetry phases that supplant the possible spin liquid states at low temperature. $NaCaNi_2F_7$ comes as a rare example that is very close to the pyrochlore Heisenberg model and is not impacted by a magneto-structural transition.

Secondly, our understanding of low-spin Heisenberg quantum spin liquids in three dimensions is very limited as they are often beyond the scope of exact or controlled approximate theoretical schemes. While there is much activity and progress in exploring quantum spin ice [16, 38, 67], which is amenable to quantum Monte Carlo (QMC) simulations [39, 68], less is understood about the quantum limit of the antiferromagnetic Heisenberg model. There is theoretical evidence that pinch point correlations survive and a quantum spin liquid phase exists [33, 34, 45, 69], but the specific character of the ground state and of the magnetic excitations is unknown. Experiments on $NaCaNi_2F_7$ are therefore an indispensable guide for our understanding of these magnets [70].

Thirdly, as we shall see in this chapter, the success of applying relatively simple methods (those we introduced in Chapter 3) to explain the dynamics of $NaCaNi_2F_7$ is as striking as it is encouraging. Our results have broader implications about the nature of quantum spin liquid dynamics, which may be applicable to other yet unexplored systems and models in this class.

The content of this chapter is arranged as follows. We first review the properties of the pyrochlore compound $NaCaNi_2F_7$. We then determine its spin Hamiltonian

and study the dynamical structure factor by three approaches—molecular dynamics (MD) simulations, the stochastic large-n (SLN) model and the linear spin wave theory (LSWT). We show that they reproduce remarkably well the momentum dependence of the experimental inelastic neutron scattering intensity as well as its energy dependence with the exception of the lowest energies.

We discuss two surprising aspects—the complete lack of sharp quasiparticle excitations in momentum space and the success of the linear spin wave theory in a regime where it would be expected to fail. The discussion leads to a natural physical picture of the spin dynamics in $NaCaNi_2F_7$. We end the chapter by discussing the roles of disorder and quantum effect in this system.

The work in this chapter is published in References [52, 59], in collaboration with Kemp W. Plumb, Hitesh J. Changlani, Allen Scheie, Jason W. Krizan, Jose A. Rodriguez-Rivera, Yiming Qiu, Barry Winn, Robert J. Cava, Collin L. Broholm, Oleg Tchernyshyov, and Roderich Moessner.

4.1 Experimental results

$NaCaNi_2F_7$ is one member of a family of recently discovered transition metal pyrochlore fluorides [71–73]. It has a structure of two interpenetrating lattices of corner-sharing tetrahedra. The magnetic Ni^{2+} ions resides on one pyrochlore lattice and an equal mixture of Na^{1+} and Ca^{2+} ions on the other to ensure overall charge

neutrality. Diffraction measurements probing the average crystal structure indicate that Na^{1+} and Ca^{2+} are uniformly and randomly distributed on equivalent lattice sites.

Magnetic susceptibility measurements show Curie-Weiss behavior with the Curie-Weiss temperature of $\theta_{CW} = 129(1)$ K [72], from which we infer the strength of the dominating nearest-neighbor exchange ~ 3 meV. The effective magnetic moment is 3.6(1) μ_B, which is consistent with $S = 1$ spins of Ni^{2+} ions [72]. Magnetic susceptibility measurements also show a spin-glass like freezing transition at $T_f = 3.6$ K. This may be explained by the charge disorder or the random strains of the Na^{1+} and Ca^{2+} distribution. For the Heisenberg pyrochlore antiferromagnet, a weak disorder in the magnetic exchange interactions leads to a spin glass transition at a temperature determined by the strength of disorder [74]. We can therefore estimate the disorder strength from the freezing temperature, with $S = 1$, $\delta J = \sqrt{3/8} k_B T_f = 0.19$ meV, which is much smaller than the dominating exchange.

The magnetic specific heat $C_m(T)$ reveals three temperature regimes of magnetism in $NaCaNi_2F_7$, see Figure 4.1(a). For $T > 18$ K, the specific heat follows what is expected from the classical spin liquid phase of the Heisenberg pyrochlore antiferromagnet [59]. Classical Monte Carlo simulation of the Heisenberg model excellently accounts for the data. In the second regime, where T is comparable with the dominant exchanges, $C_m(T)$ falls below the classical Heisenberg model. The broad maximum around 18 K indicates a crossover from classical to quantum spin liquid

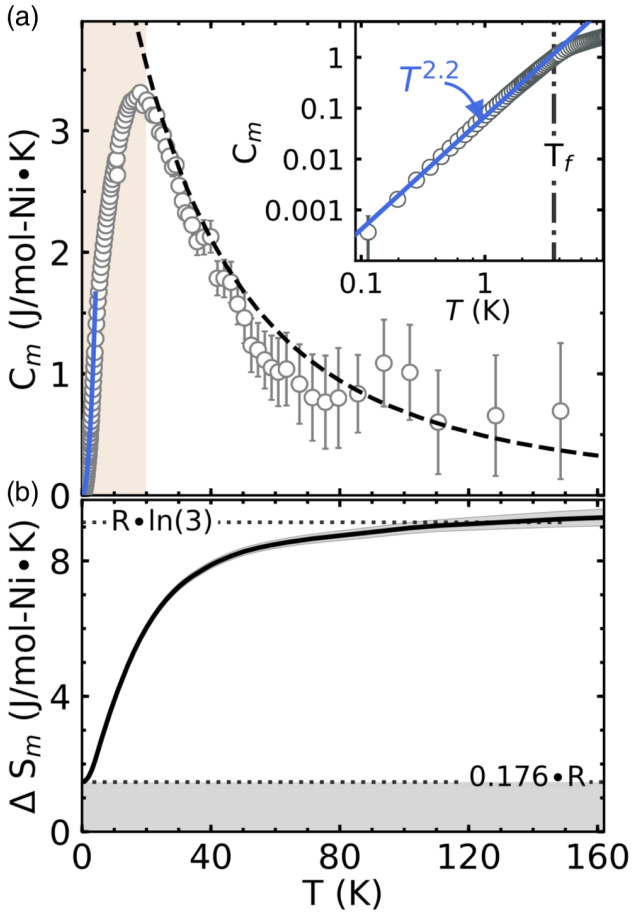

Figure 4.1: (a) Magnetic specific heat. Dashed line is from the classical Monte Carlo simulation. Light shading indicates the classical to quantum crossover regime. The inset shows the low temperature region. The solid line is a fit to $C_m(T) = AT^{\alpha}$, with $A = 0.07(1)$ and $\alpha = 2.2(1)$. (b) Magnetic entropy obtained by integration of C/T with a $0.176k_B$/spin residual entropy.

state. Finally, for $T < T_f = 3.6$ K, a discontinuity in $dC_m(T)/dT$ (see inset of Figure 4.1(a)) indicates spin freezing [72]. Figure 4.1(b) shows the magnetic entropy recovered between 100 mK and 150 K that saturates at 84% of the total $Nk_B \ln 3$. The residual entropy at 100 mK can be interpreted as the result of broken ergodicity because of the spin freezing. Specifically, A metastable spin configuration could be

kinetically arrested by the disorder potential so the material no longer explores all states of a given energy. Correspondingly we expect spin correlations for the energy range $E < k_B T_f \sim 0.3$ meV to reflect a disorder dominated regime. No long-range magnetic order is found down to 0.35 K.

Despite the spin freezing transition, quantum fluctuations dominate the system in the low temperature limit [59, 75]. In neutron scattering, by comparing the spectral weight for elastic ($E < 0.7$ meV) and inelastic scattering ($0.7 < E < 14$ meV) we find around 90% of the magnetic scattering is inelastic at $T = 1.8$ K, which greatly exceeds the $S/(S+1) = 50\%$ mark for a semi-classical ground state for spin-1 Ni^{2+} ions. This is a direct evidence that quantum fluctuations dominate the dynamics of this spin system. Integrating the dynamic structure factor $\mathcal{S}(\mathbf{q}, \omega)$ over momentum and energy, including the elastic diffuse magnetic scattering, yields a total spectral weight consistent with the $3.7\mu_B$ effective magnetic moment extracted from the high temperature magnetic susceptibility data [72].

No energy gap has been detected in the inelastic scattering spectrum. An upper bound for the gap is set by the resolution of the measurement 0.17 meV. The magnetic excitations form a continuum of inelastic scattering over an energy bandwidth of roughly 12.5 meV, with low energy pinch points and finite energy maxima (of the order of the Heisenberg exchange). For more on the dynamical structure factor, see Section 4.4.

These results demonstrate that disorder can act to only freeze the lowest energy

magnetic degrees of freedom; at higher energies, a magnetic excitation continuum characteristic of fractionalized excitations persists.

4.2 Spin Hamiltonian

We determine the Hamiltonian by fitting the static structure factor $\mathcal{S}^{\mu\nu}(\mathbf{q})$. For a given spin Hamiltonian in the paramagnetic state at a finite temperature, the static structure factor can be calculated by the stochastic large-n model as in Equation (3.15). To compare with neutron cross section, we convert the static structure factor to the intensity

$$I(\mathbf{q}) = r_0^2 \left| \frac{g}{2} f(q) \right|^2 \sum_{\mu\nu} \left(\delta_{\mu\nu} - \frac{q_\mu q_\nu}{q^2} \right) \mathcal{S}^{\mu\nu}(\mathbf{q}), \tag{4.1}$$

where $r_0 = 0.539 \times 10^{12}$ cm is the magnetic scattering length, $f(q)$ is the magnetic form factor for Ni^{2+} [76], and g is the isotropic g-factor.

Experimentally, the static structure factor is obtained by integrating the magnetic neutron scattering intensity over the energy range $0 < E < 14$ meV at $T = 1.8(2)$ K.

Detailed information is provided by polarized neutron scattering. Vertical field polarized neutron measurements have the non-spin-flip (NSF) channel, which measures components of the dynamic spin correlation function that are perpendicular to the horizontal scattering plane, and spin-flip channel (SF), which measures the component of the dynamics spin correlation function polarized within the scattering plane and perpendicular to momentum transfer.

Without further analysis, the similarity of SF and NSF magnetic neutron intensities in Figure 4.2(a) indicates a near spin-space isotropic system. Weak anisotropic interactions are revealed by two features of the polarized intensity. First, the SF scattering exhibits a pronounced asymmetry of the lobes of intensity around $(\pm 0.6, \pm 0.6, 2)$ positions. Second, the NSF intensity is diminished around the $(0, 0, 2)$ pinch point positions.

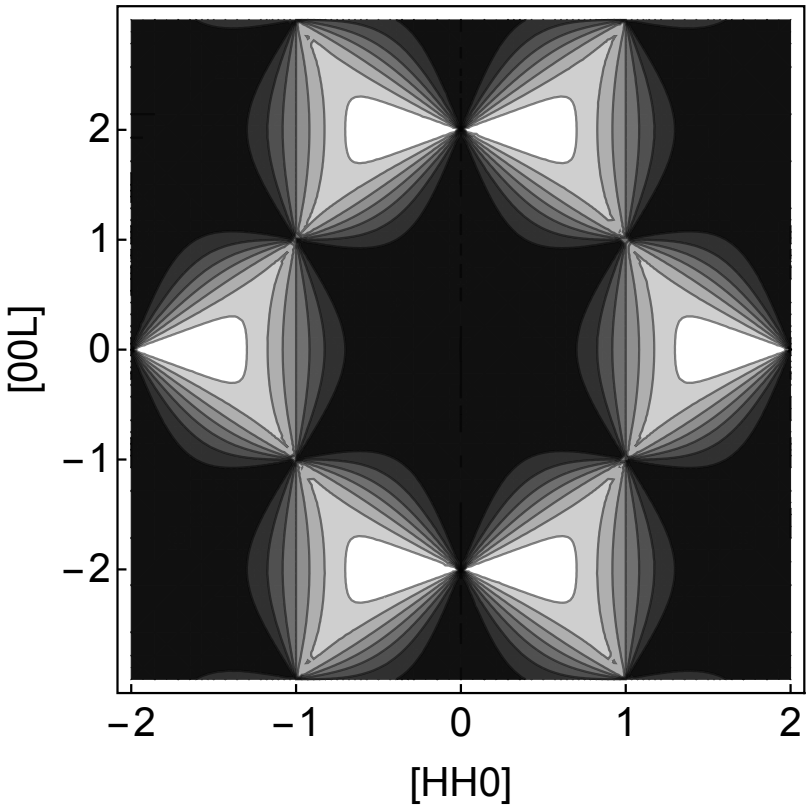

Figure 4.2: Static structure factor from (a) integrating the (symmetrized) inelastic neutron scattering data over energy, (b) SLN calculation with the best fit of exchange parameters, and (c) Monte Carlo simulations with the same parameters.

We allow five free exchange parameters in the fit—all four parameters in the full symmetry allowed nearest-neighbour bilinear exchange Hamiltonian and an isotropic

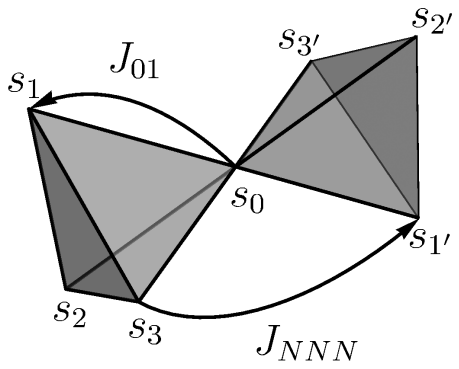

Figure 4.3: Nearest-neighbor and next-nearest neighbor interactions. In the fitting for $NaCaNi_2F_7$, J_{NNN} is isotropic and J_{01} between different global spin components is expressed in Equation (2.4).

next-nearest neighbor (denoted by double angle brackets) interactions. The Hamiltonian is thus in the form of

$$H = \sum_{\langle ij \rangle} \sum_{\mu\nu} J_{ij}^{\mu\nu} s_i^\mu s_j^\nu + \sum_{\langle\langle ij \rangle\rangle} \sum_{\mu\nu} J_{NNN} \delta_{\mu\nu} s_i^\mu s_j^\nu \tag{4.2}$$

in the global frame for spins, where the matrix J_{01}, for example, is given in Equation (2.4). As a starting point, we begin with the estimation provided by the Curie-Weiss temperature, which is compatible with isotropic Heisenberg exchange of 3 meV between nearest neighbors. We find the best global fit of the measured static structure factor in SLN for the exchange parameters: $J_1 = J_2 = 3.2(1)$ meV, $J_3 = 0.019(3)$ meV $J_4 = 0.070(4)$ meV and $J_{NNN} = 0.025(5)$ meV. The resulting calculated neutron intensity is shown in Figure 4.2(b). We find that the model agrees exceptionally well with the experiment, reproducing the above-mentioned details in the polarized data.

Classical Monte Carlo simulations provide a further check. By using the determined exchange parameters as input into Monte Carlo simulations, the static struc-

ture factor is calculated for typical spin configuration samples. The results are shown in Figure 4.2, in comparison with the measured static structure factor and that calculated from SCGA.

We conclude that the spin Hamiltonian for $NaCaNi_2F_7$ closely approximates the $S = 1$ Heisenberg antiferromagnet on the pyrochlore lattice, perturbed only at the percent level by nearest-neighbor exchange anisotropies, next-nearest neighbour interactions, and exchange disorder.

Although SLN predicts that small perturbations in the classical Heisenberg model result in a magnetically ordered state, Monte Carlo simulations for the anisotropic Hamiltonian relevant to $NaCaNi_2F_7$ (without exchange disorder) find no magnetic order above $T = 0.5$ K. In addition, these perturbations are significantly smaller than the strength of the exchange disorder. So, even if the disorder free Hamiltonian for $NaCaNi_2F_7$ ultimately has long range magnetic order, it is preempted by spin freezing from exchange disorder.

4.3 Disordered ground state

To get a sense of the ground state of $NaCaNi_2F_7$ considering the nearly ideal Heisenberg exchange Hamiltonian and the frozen magnetism, we run Monte Carlo simulations to find the energy minima. We find the energy-optimized spin configurations for the bond-disordered Heisenberg Hamiltonian with small anisotropic

exchanges relevant to $NaCaNi_2F_7$ mostly satisfy the condition $\sum_{i\in\boxtimes} \mathbf{s}_i = 0$.

For a tetrahedron, the doublet of bond operators (f_1, f_2) defined by

$$\begin{aligned} f_1 &= \frac{1}{2\sqrt{3}}(\mathbf{s}_0\cdot\mathbf{s}_1 - 2\mathbf{s}_0\cdot\mathbf{s}_2 + \mathbf{s}_0\cdot\mathbf{s}_3 + \mathbf{s}_1\cdot\mathbf{s}_2 - 2\mathbf{s}_1\cdot\mathbf{s}_3 + \mathbf{s}_2\cdot\mathbf{s}_3), \\ f_2 &= \frac{1}{2}(\mathbf{s}_0\cdot\mathbf{s}_3 + \mathbf{s}_1\cdot\mathbf{s}_2 - \mathbf{s}_0\cdot\mathbf{s}_1 - \mathbf{s}_2\cdot\mathbf{s}_3), \end{aligned} \tag{4.3}$$

provides an economical characterization of the particular spin configuration inside the $\sum_{i\in\boxtimes} \mathbf{s}_i = 0$ manifold [66, 77, 78].

The statistical distribution extracted from Monte Carlo simulations are shown in Figure 4.4, where possible values span an equilateral triangle in the (f_1, f_2) plane. Coplanar states with pairs of antiparallel spins lie along the edges and collinear spin configurations are at the vertices. The classical Heisenberg (only) model with weak

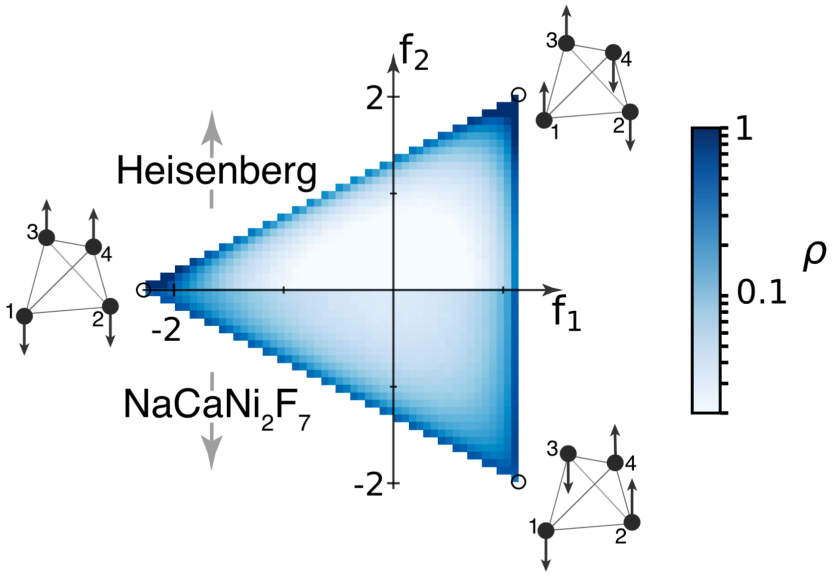

Figure 4.4: Histogram of the bond order parameter (f_1, f_2) from classical Monte Carlo simulations for Heisenberg and exchange model relevant to $NaCaNi_2F_7$ including exchange disorder. Extremal spin configurations corresponding to collinear spin arrangements are shown.

bond disorder is glassy [73] and exhibits a tendency to form locally collinear states [79]. Relatively, the probability density is enhanced along the boundaries and away from the corners in $NaCaNi_2F_7$. This indicates a tendency to form configurations of pair-wise collinear spins when the small anisotropic interactions specific to $NaCaNi_2F_7$ are added, while all of the $\sum_{i\in\boxtimes} \mathbf{s}_i = 0$ manifold is accessible for the ground state.

4.4 Dynamical structure factor

We next analyze the magnetic excitation spectrum. We calculate the dynamical structure factor

$$\mathcal{S}(\mathbf{q},\omega) = \sum_{\mu\nu}(\delta_{\mu\nu} - \frac{q_\mu q_\nu}{q^2})\mathcal{S}^{\mu\nu}(\mathbf{q},\omega), \tag{4.4}$$

with the three methods introduced in Chapter 3: firstly, molecular dynamics (MD) simulations of the pyrochlore magnet [22], where the classical Landau-Lifshitz equations of motion for the spins are integrated numerically and averaged over initial conditions obtained from Monte Carlo simulations at temperature $T = 1.8$ K; secondly, linear spin-wave theory (LSWT) to describe spin dynamics near a low-energy state with a similar averaging over initial conditions; thirdly, a self-consistent Gaussian approximation adapted to frustrated magnets [80] and extended into a stochastic model [47], which we refer to as stochastic large-n (SLN). For definitions of $\mathcal{S}^{\mu\nu}(\mathbf{q},\omega)$ in different methods, see Equations (3.8) and (3.41).

We rescale the two "classical" approaches MD and SLN by a factor $\omega/(k_B T)$,

which crudely reproduces the effects of quantum fluctuations at low temperatures.

The comparison between the experimental data and the dynamical structure factor calculated from the three theoretical methods is shown from different view angles in the following figures.

Figure 4.5 displays momentum dependence of the dynamical structure factor through a series of constant energy transfer slices in the [HHL] and [H0L] planes. At low energies, a bow-tie pattern with pinch points characteristic of a $U(1)$ spin liquid are clearly visible. Their presence implies that each tetrahedron has vanishing total magnetization [20,81]. From the quantum-mechanical perspective, however, adjacent tetrahedra cannot both be in $S = 0$ states, as their total spin operators do not commute. Therefore, while for the classical theories, the pinch points sharpen as $\sqrt{T}$ when T is lowered [82], for $S = 1/2$ they were found to be quite smeared out [83], becoming sharper as S increases. For $S = 1$, a prediction for the full-width at half maximum of the pinch point in the static correlations at [002] of $\delta q_{\mathrm{PP}}^{\mathrm{FWHM}} = 4\pi/3$ [33] is comparable to the value $\approx \pi$ extracted form the low-T experimental data.

At higher energies, the overall intensity distribution changes little at first, but whatever sharp features present at low energies are washed out. The intensity minimum in the scattering rhombus around [202] is slowly filled in and the pinch points broaden. At higher energies, phonons pollute the experimental signal at large $\mathbf{q}$, but a rearrangement of the weight is still discernible, especially in the [HHL]-plane data. The momenta around the pinch-point develop prominent pairs of "half-moons" at 8

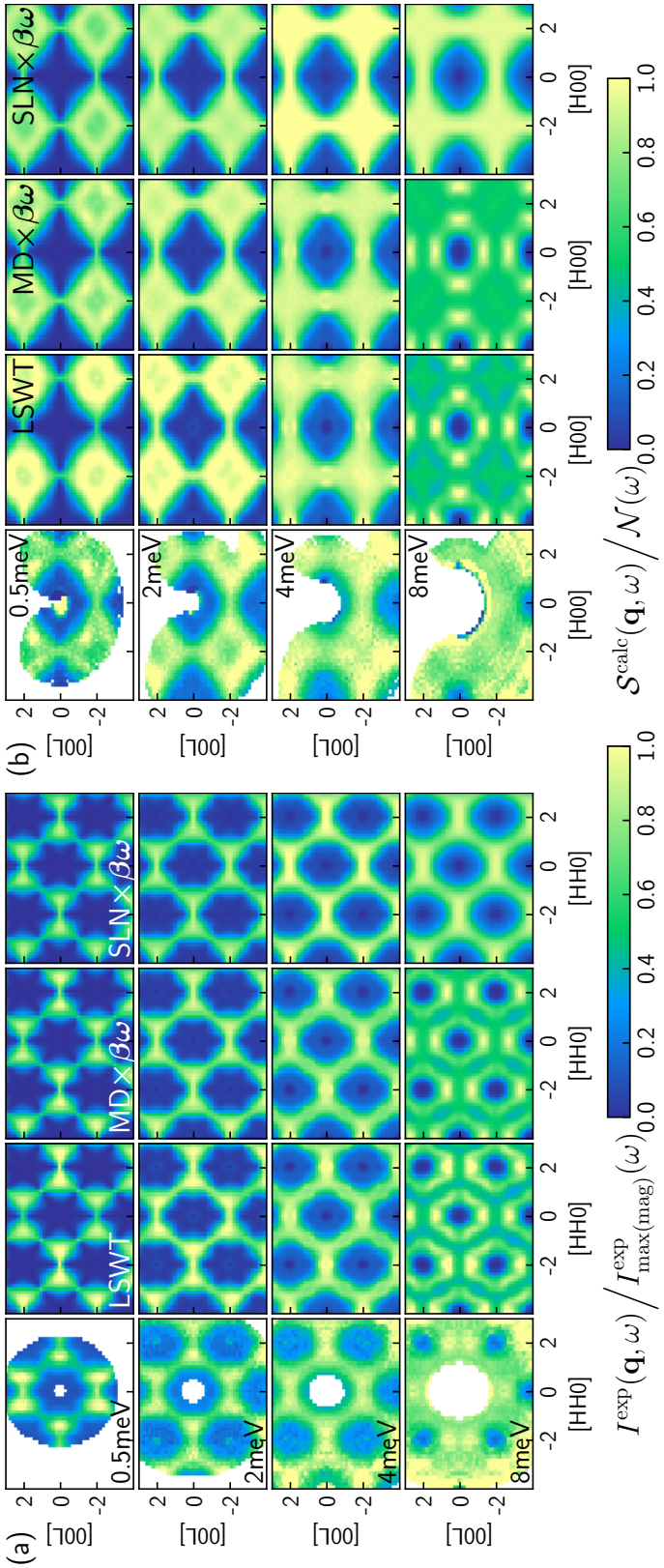

Figure 4.5: Dynamical structure factor in (a) [HHL] and (b) [H0L] planes at constant energies: experiment compared to linear spin wave theory, molecular dynamics, and the stochastic model. Data in (a) were collected on CNCS and in (b) on MACS. Raw neutron intensity has been corrected by the magnetic form-factor for Ni^{2+} [76]. To focus on wavevector dependence, data are rescaled for each value of energy, for experiment, by the maximum magnetic scattering intensity; and by the maximum intensity in the MD simulations for the six theory panels, with an additional factor $\beta\omega$ between MD/SLN and LSWT, $\mathcal{N}(\omega) = \beta\omega\mathcal{S}^{\mathrm{MD}}_{\mathrm{max}}(\omega)$, see Equation (3.47).

meV, a dispersing complement to the pinch points [84, 85]. This feature is present in MD and LSWT, but not in SLN, which is relaxational and does not capture spin precession.

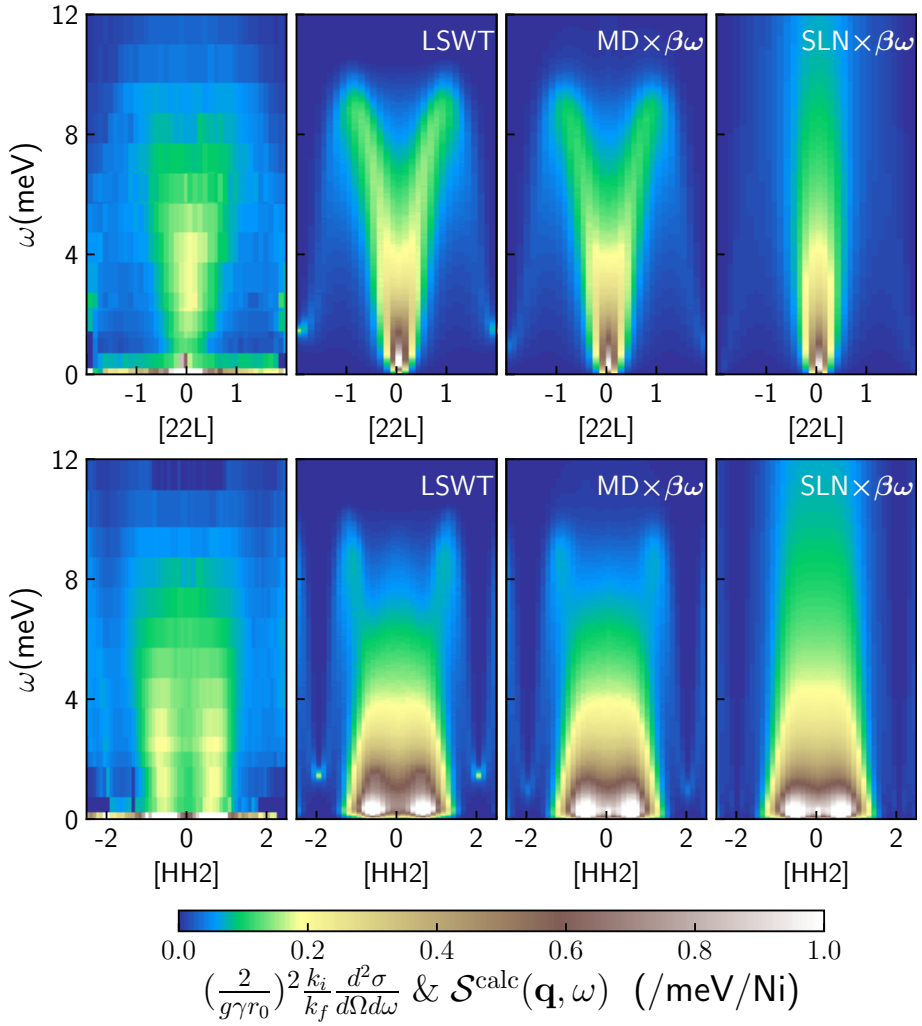

Figure 4.6: Energy dependence of dynamical structure factor along momentum cuts [22L] and [HH2]. Neutron scattering intensity is in absolute units.

We next turn to the energy dependence of the data, Fig. 4.6, along two momentum paths [22L] and [HH2]. The general shapes of experiment and MD and LSWT are

very similar—a broad signal with a vertical appearance reminiscent of a fountain. SLN fails to capture the high-energy structure, which can therefore be ascribed to the precessional spin dynamics not captured by this method; otherwise, the theory plots are consistent.

We supplement the color plots by a quantitative comparison of the dynamical

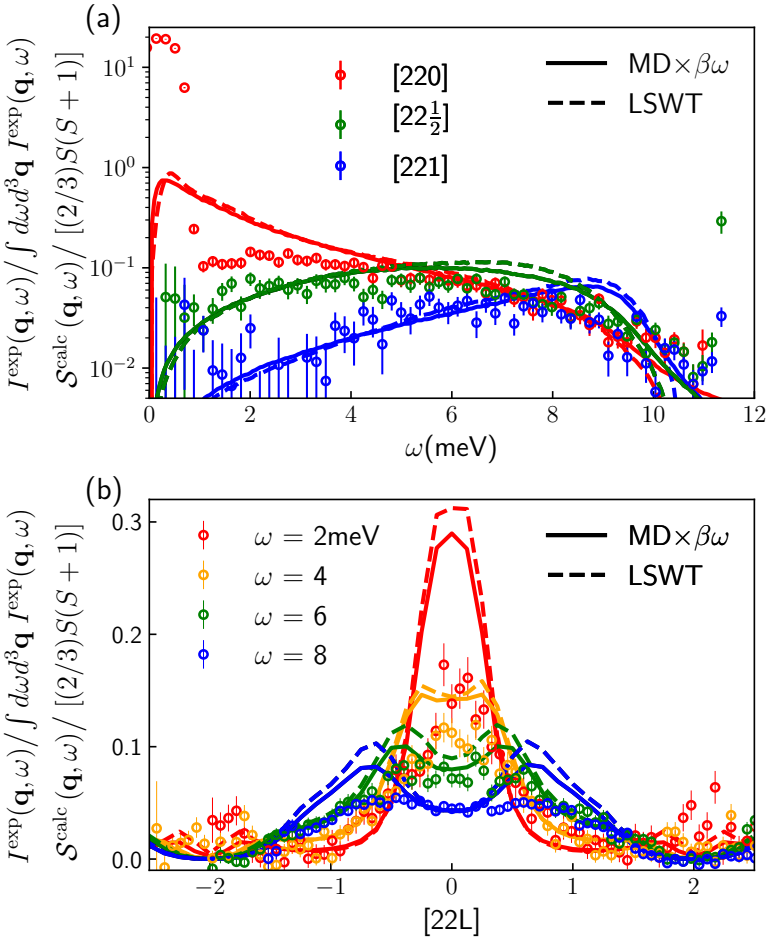

Figure 4.7: Line cuts of dynamical structure factor and quantitative comparison between experiment and MD/LSWT. (a) Energy-dependence at $\mathbf{q} = [220]$, $[22\frac{1}{2}]$ and [221]. Log scale is used for the y-axis to include the quasi-elastic signals. (b) Momentum dependence along [22L] at $\omega = 2,4,6$ and 8meV. The neutron scattering intensity $I^{\text{exp}}(\mathbf{q},\omega)$ is background subtracted. See text for normalization of data.

structure factor between the experiment and MD and LSWT calculation, see Figure 4.7. For comparison, all data are normalized as follows. For the neutron data, background contributions from incoherent nuclear scattering and scattering from the sample environment are subtracted and the intensity is normalized by the total spectral weight $\int d\omega d^3\mathbf{q}\, I^{\mathrm{exp}}(\mathbf{q},\omega)$. MD (solid lines) and LSWT (dashed lines) data $\mathcal{S}^{\mathrm{calc}}(\mathbf{q},\omega)$ are divided by $(2/3)S(S+1)$, assuming isotropic magnetic moment. In the constant energy cuts, the dynamic structure factor is peaked at finite energy transfers and very broad (in the order of J_1) dispersive ridges are observed.

The largest disagreement between theory and experiment occurs at low frequencies, especially around [220]. Near 1 meV, there exists a large suppression of the inelastic neutron scattering intensity compared with theoretical calculations. A large increase of the experimental signal below 1 meV is not reflected in theory either.

To conclude, our three complementary theoretical approaches reproduce well the dynamical structure factor $\mathcal{S}(\mathbf{q},\omega)$ from inelastic neutron scattering for all momenta $\mathbf{q}$ and for a broad range of energies ω; the quality of the agreement differs between methods at the highest energies. At low energies, we find the well-known pinch-point motifs; at intermediate energies, characteristic structures complementary to the pinch points appear [84,85]. Overall, the main disagreement between experiment and theory appears at the lowest energies.

4.5 Spin dynamics of $NaCaNi_2F_7$

To get an understanding of the spin dynamics of $NaCaNi_2F_7$, we try to address the remarkable agreement between theory and experiment (with the exception of the lowest energies), as well as the agreement between the two methods MD and LSWT. The latter is quite unexpected, for several reasons. First, the absence of a state with long-range order around which to perturb, the existence of which would have guaranteed a Goldstone mode as a long-lived magnon excitation. Other models without long-range order, such as the $S = 1/2$ and 1 Heisenberg chains, show a breakdown of LSWT, as their respective low-energy descriptions involve not the gapless magnons but either fractionalized $S = 1/2$ spinons or Haldane's gap. Second, one might expect considerable quantum renormalization effects from the small spin length $S = 1$, all the more so since the classical local exchange field is reduced as a result of geometric frustration. Third, a finite fraction of the spin-wave modes live at or near zero energy in LSWT, which implies the onset of the many-particle continuum already at the bottom of the single-particle spectrum. Above this onset, spin waves are expected to show damping [86].

Here, LSWT actually finds another route to work: it is not a theory of universal low-energy hydrodynamic excitations, but of the statistically typical behavior at short time (high energies) scales, which fails at long times (low energies), thus in the end conforming to at least a subset of the above expectations.

To see this, think of the (near-)zero frequency modes as responsible for "slow" mo-

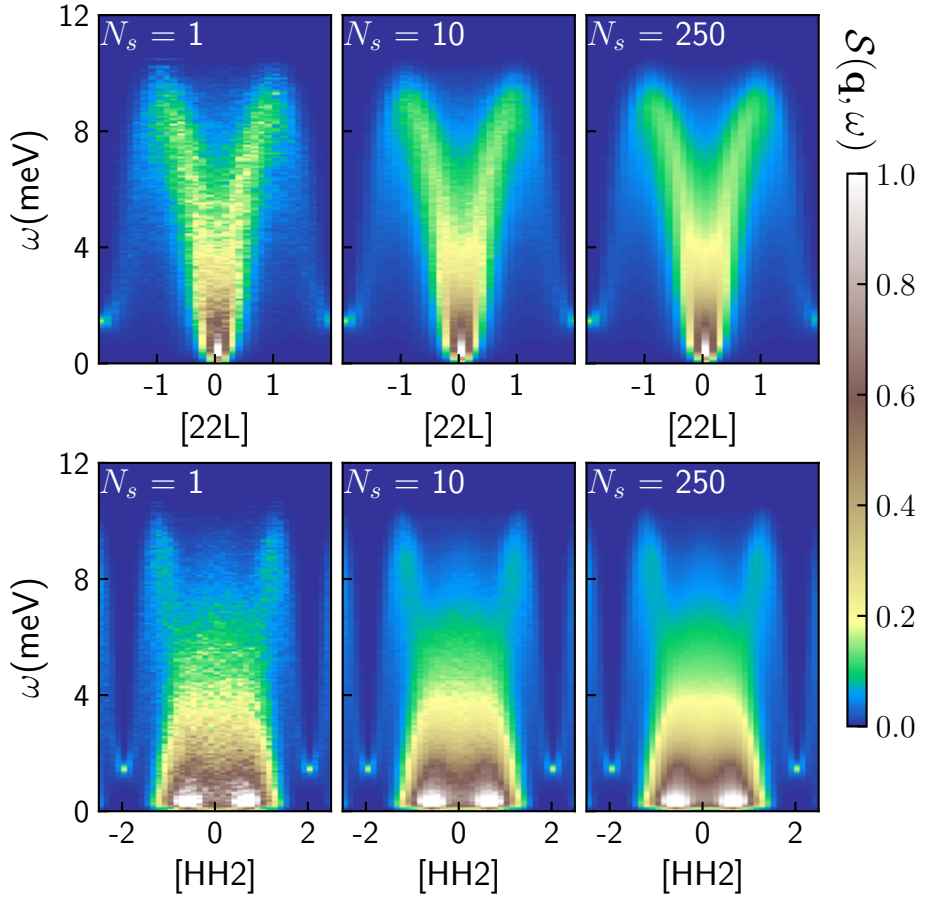

Figure 4.8: Real space linear spin wave theory results for different numbers of Monte Carlo samples N_s with $L=8$ (b).

tion between (near-)degenerate ground states, and of "fast" oscillatory spin waves—with finite frequency and scattering rates—around these as driving this motion [22, 23, 47]. Statistically, the spectra of these fast oscillations appear not to change as the slow modes evolve, making the broad finite-frequency spectra we consider here effectively time-independent. Indeed, we do find self-averaging in practice as only a few configurations are needed to obtain smooth spectra for large system sizes, see Figure 4.8. This is consistent with weak disorder in the dynamical matrix, since they

occur mainly in off-diagonal terms, with the diagonal exchange field nearly uniform. As expected for weak disorder in three dimensions, spin waves away from the band edges are delocalized. We diagnose this by the scaling of their inverse participation ratio (IPR).

In analogy to the density distribution $\rho_e(\mathbf{r}) = |\psi_e(\mathbf{r})|^2$ of a given electron wavefunction, which is normalized $\int d^3\mathbf{r}\, \rho_e(\mathbf{r}) = 1$, we consider the normalization (3.35) and define the density distribution of the spin wave modes at energy ω_α to be

$$\rho_\alpha(\mathbf{r}_i) = (\psi_\alpha^i)^\dagger(-i\Gamma_2)\psi_\alpha^i, \tag{4.5}$$

where $\Gamma_2 = \begin{pmatrix} 0 & -1 \\ 1 & 0 \end{pmatrix}$ and $\psi_\alpha^i \equiv ([\psi_\alpha]_{2i}, [\psi_\alpha]_{2i+1})^T$, corresponding to the two transverse spin deviations from the equilibrium direction. The IPR is given by

$$\mathrm{IPR}(\omega_\alpha) \equiv \sum_{i=1}^{N} |\rho_\alpha(\mathbf{r}_i)|^2. \tag{4.6}$$

For a delocalized mode, we expect $\mathrm{IPR}(\omega_\alpha) \sim O(1/N)$ while for a localized mode $\mathrm{IPR}(\omega_\alpha) \sim O(1)$. Fig. 4.9 shows the IPR multiplied by the number of sites, i.e. $N \times \mathrm{IPR}(\omega)$. The collapse of the values for different lattice sizes (except perhaps at the edges of the spectrum, especially the upper edge) indicates a delocalized character of spin wave modes for a wide energy energy range.

The statistical behavior of the spin waves also explains why spin-wave scattering does not invalidate the picture. Normally magnons have a well-defined momentum and energy, so a measurement of the dynamical structure factor $\mathcal{S}(\mathbf{q}, \omega)$ produces sharp features. In a disordered state, spin waves can have a well-defined energy but

not momentum, so LSWT predicts a broad continuum of $\mathcal{S}(\mathbf{q}, \omega)$ at a given ω. Any further broadening of an individual mode due to its finite lifetime is small in temperature T, and therefore parametrically smaller than the largely T-independent total bandwidth. Thus, unlike in the case of an initially sharp mode, lifetime broadening is insignificant.

In the low-T limit, zero modes have no dynamics in LSWT (their frequency is zero). Motion along the ground-state manifold is thus frozen out and LSWT fails to capture their motion arising from scattering off high-energy excitations, which is present in MD and SLN theories. It is thus clear that our comparison is not particularly sensitive to the details of the low-frequency physics.

The analysis above leads to a physical picture for the spin dynamics of $NaCaNi_2F_7$. There are many degenerate or nearly degenerate ground states with similar excitation spectrum, which can be described by delocalized spin waves at finite frequencies. They

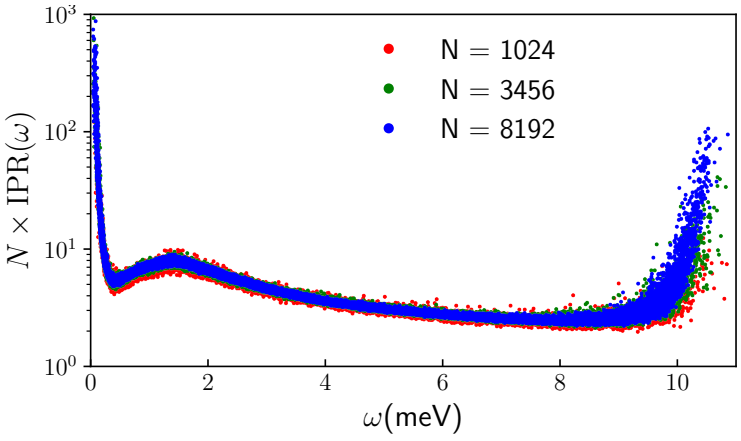

,

Figure 4.9: Inverse participation ratio (IPR) of the normalized real-space spin wave modes $\psi(\mathbf{r}, \omega)$ as a function of frequency for different system sizes. The modes are delocalized everywhere except for possibly at the edges of the spectrum.

interact with the soft modes and mediate the exploration of the system among all the degenerate ground states.

4.6 Discussion

Typically, the universal low-energy features of spin liquid ground states are topological in nature and as such invisible to experimental probes that couple to local correlations [6]. Indeed, it has been a common recent theme in quantum magnets that the structure factor *away from* low energies is most instructive. While this part of the spectrum is not universal, and may not contain enough information to pin down the nature of the quantum spin liquid unambiguously, it permits simple modeling and detailed comparison with experiments (e.g., of deconfined spinons for weakly coupled Heisenberg chains [87]).

Furthermore, the presence of disorder and freezing [75, 88] likely renders the low-energy features fragile, thus requiring additional modeling [89].

More generally, further small terms in the Hamiltonian, potentially missed by our fitting procedure, may redistribute low-energy spectral weight, and even lead to a conventional ordered state at the lowest temperatures; in this case, the modelling presented here applies to the proximate spin liquid regime at temperatures or energies above the small transition energy scale. Finally, an accurate treatment of low-energy features requires going beyond the simple version of our classical-quantum

correspondence factor $\beta\omega$.

All these complications should not distract from an important feature seen in experiment and reproduced in theory: the complete absence of sharp quasiparticle peaks characteristic of magnons with well-defined momenta and energies. It reflects the spatially disordered nature of the spin configurations in our classical theory and raises the question about the appropriate description of the corresponding low-temperature quantum state.

The final basic issue raised by our study is the role of the "quantumness" in this compound. The success of classical and semi-classical modeling across a broad range of energies, at temperatures far below the Curie-Weiss scale, is rather unexpected.

The low-energy discrepancies discussed above seem like a small price to pay for the great simplicity of our theoretical approaches. This calls for experiments on analogous compounds with larger spins, where we expect the low-energy regime to be better modeled while retaining the medium- to high- energy features already successfully accounted for.

Indeed, this expectation is fulfilled by a very recent study of another pyrochlore antiferromagnet $MgCr_2O_4$, which is a system of $S = 3/2$ spins. In Reference [65], Bai et. al. demonstrate that $MgCr_2O_4$ in its cooperative paramagnetic regime can be described by a Heisenberg model with exchange interactions up to third-nearest neighbors. There, real space linear spin wave calculations faithfully reproduced the dynamical structure factor measured in experiments at all momentum and energy.

Similar conclusions are drawn about the spin dynamics—spin waves propagating in a highly-correlated paramagnetic background.

Employing semi-classical modelling for what is expected to be a quantum spin liquid is not without precedent. This was done for the Kitaev honeycomb model [40], whose exact solvability allows for a reliable comparison in detail [90]. There [91], the high-frequency portion of the response was accounted for, with a reasonable amount of data post-processing, while the physics related to the emergent fluxes at low energies—the most direct manifestation of fractionalization—remained inaccessible.

Similarly, qualitative signatures of a quantum spin liquid may be visible only at the lowest energies. If so, the challenge is to explain a rapid crossover into a classical regime, where quantum mechanics mainly enters in the mode occupation numbers. An alternative would be the absence of a qualitatively distinct low-frequency quantum spin liquid regime altogether. This could either happen intrinsically, if the emergent low-energy description is amenable to a semi-classical description; or extrinsically, in that the quantum spin liquid behavior is so fragile that disorder or coupling to phonons destroy it entirely.

Chapter 5

Conclusion

The discovery of new phases of matter has been a long and fruitful pursuit in condensed matter physics. Quantum spin liquids are among the most intriguing ones. Geometric frustrations and quantum fluctuations are predicted be able to drive a system into an exotic magnetic state with no long-range magnetic order even in the zero temperature limit. But because of the lack of local features in their ground states, their identification in experiments is very challenging. This dissertation is an example of the effort in bridging theoretical models and experimental observations by studying the excitation spectrum of a quantum spin liquid candidate.

By using three complementary methods—stochastic model, molecular dynamics and linear spin wave theory, we have explored the precessional and relaxational dynamics of the perturbed Heisenberg model on a pyrochlore lattice. Our approaches have turned out to be a successful modeling for the excitations in the three dimen-

sional spin-1 quantum spin liquid candidate $NaCaNi_2F_7$. Our understanding of spin dynamics in the system—a combined picture of the statistics of spin wave excitations and the exploration of the system among many ground states—is quite natural for a highly frustrated magnet. It also applies to another classical spin liquid candidate, the pyrochlore compound $MgCr_2O_4$ in its low temperature paramagnetic phase.

Our attempt to mimic quantum effects in the system by considering Bose-Einstein statistics of spin wave modes is a practical success. But theories fail to qualitatively agree with experiments at the lowest-energy regime. Better methods to capture quantum fluctuations in the Heisenberg model are urgently needed. It also raises the broader question, to what extend and under what circumstances classical or semi-classical models for spin dynamics are effective to describe a system of quantum-mechanical nature.

Appendix A

Classical order parameters

The point group of the pyrochlore lattice is T_d. Take the above-mentioned tetrahedron centered at the origin and embed it in a cube. The point group T_d has following symmetry operations: threefold rotations (C_3) about the four body diagonals ([111]), twofold rotations (C_2) and fourfold improper rotations (S_4) about $\mathbf{x}, \mathbf{y}$ and $\mathbf{z}$ axis ([100]), and mirror reflections with respect to the six diagonal planes (110). For equivalence classes of symmetry operations and irreducible representations of T_d, see Table A.1.

We have seen in Chapter 2 that the lattice symmetry analysis can reduce the number of free parameters for spin interactions. Another nice little exercise is to derive the order parameters for classical spins from the representation theory of the symmetry group.

Let $\mathbf{a} = (\mathbf{s}_0, \mathbf{s}_1, \mathbf{s}_2, \mathbf{s}_3)^T$. In the global coordinate frame, a simple choice of the

T_d	E	$8C_3$	$3C_2$	$6S_4$	$6\sigma_d$
A_1	$+1$	$+1$	$+1$	$+1$	$+1$
A_2	$+1$	$+1$	$+1$	-1	-1
E	$+2$	-1	$+2$	0	0
T_1	$+3$	0	-1	$+1$	-1
T_2	$+3$	0	-1	-1	$+1$
$\mathrm{Tr}R_a$	12	0	0	0	-2
$\mathrm{Tr}R_p$	12	0	0	0	$+2$

Table A.1: Character table for point group T_d. The last two rows are the traces of the reducible representations of an axial and a polar vector.

basis is $\{\mathbf{a}^\alpha, \alpha = 1, \ldots, 12\}$ with $(\mathbf{a}^\alpha)_\alpha = 1$ and $(\mathbf{a}^\alpha)_{\beta\neq\alpha} = 0$. For our purpose, it is adequate to compute the representation matrix for one operation out of each equivalence class, see Table A.1.

First, a spin transforms like an axial vector. The spin part of the linear transformation matrices (R_s) directly follows the definition of symmetry operations acting on a spin located at the origin $\mathbf{s} = (s^x, s^y, s^z)$.

Second, for the lattice part, the point group T_d is nothing but a permutation group for the four corners of a tetrahedron. We can construct the representation matrices (R_t) by observing the permuting rule of the labeled corners under symmetry operations.

Third, the direct product of the two sets of matrices $R_a = R_t \otimes R_s$ is the full

representation on basis **b**. The traces of these matrices are listed in the second last row of Table A.1. We can now conclude that our representation comprises 5 irreducible representations (irreps) $R_a = A_2 + E + 2T_1 + T_2$.

Finally, we need to identify the invariant subspaces from the basis **b**. It is technically nontrivial to block diagonalized all matrices simultaneously, but we can make quite reliable guesses. For example, since the three-dimensional T_1 irreps (T_{1A} and T_{1B}) transform like angular momenta, one of them is the collinear ferromagnetic states with $s_i^\mu = 1$ and $s_i^{\nu\neq\mu} = 0$. The ordered spin ice manifold, which has a nonvanishing total moment, is thus the linear combination of the two.

We summarize the classical order parameters [13, 92] and list the coefficients on basis $\{\mathbf{a}^\alpha\}$ in Table A.2.

The order parameters fully describe the classical phase if the spin state on a pyrochlore lattice orders with wavevector $\mathbf{q} = 0$ (the magnetic unit cell is still one tetrahedron). When there is no magnetic order or an exotic order, the order parameters can also serve as a useful local characterization.

Irrep	Factor	s_0^x	s_0^y	s_0^z	s_1^x	s_1^y	s_1^z	s_2^x	s_2^y	s_2^z	s_3^x	s_3^y	s_3^z	Phase
A_2	$1/2\sqrt{3}$	$+1$	$+1$	$+1$	$+1$	-1	-1	-1	$+1$	-1	-1	-1	$+1$	All-in-all-out
E	$1/2\sqrt{2}$	$+1$	0	-1	$+1$	0	$+1$	-1	0	$+1$	-1	0	-1	Γ_5
	$1/2\sqrt{6}$	$+1$	-2	$+1$	$+1$	$+2$	-1	-1	-2	-1	-1	$+2$	-1	
T_{1A}	$1/2$	$+1$	0	0	$+1$	0	0	$+1$	0	0	$+1$	0	0	Collinear FM
	$1/2$	0	$+1$	0	0	$+1$	0	0	$+1$	0	0	$+1$	0	
	$1/2$	0	0	$+1$	0	0	$+1$	0	0	$+1$	0	0	$+1$	
T_{1B}	$1/2\sqrt{2}$	0	$+1$	$+1$	0	-1	-1	0	-1	$+1$	0	$+1$	-1	Non-collinear FM
	$1/2\sqrt{2}$	$+1$	0	$+1$	-1	0	$+1$	-1	0	-1	$+1$	0	-1	
	$1/2\sqrt{2}$	$+1$	$+1$	0	-1	$+1$	0	$+1$	-1	0	-1	-1	0	
T_2	$1/2\sqrt{2}$	$+1$	-1	0	-1	-1	0	$+1$	$+1$	0	-1	$+1$	0	Palmer Chalker
	$1/2\sqrt{2}$	$+1$	0	-1	-1	0	-1	-1	0	$+1$	$+1$	0	$+1$	
	$1/2\sqrt{2}$	0	$+1$	-1	0	-1	$+1$	0	-1	-1	0	$+1$	$+1$	

Table A.2: Classical order parameters and magnetic phases with ordering wavevector $\mathbf{q} = 0$.

Appendix B

Applicability of stochastic model

According to the critical behavior of the system at β_c, the solution for $\lambda(\beta_c, N)$ to Equation (3.6) approaches the thermodynamic limit $\lambda_0 = \lim_{N\to\infty} \lambda(\beta_c, N)$ as a power law with respect to the length scale,

$$\lambda(\beta_c, N) - \lambda_0 \propto N^{-\alpha/3}. \tag{B.1}$$

We can give a good estimation for the lower bound for the value of λ_0, that is, to tune the Boltzmann factor (3.3) to be positive definite, $\lambda_0 > -\mathrm{Min}\{\epsilon_\rho(\mathbf{q})\} > 0$, like a chemical potential.

The power law relation can be investigated by taking

$$\Delta(\beta, N_1, N_2) = -3\frac{\ln\left[\lambda(\beta, N_1) - \lambda_0\right] - \ln\left[\lambda(\beta, N_2) - \lambda_0\right]}{\ln N_1 - \ln N_2}, \tag{B.2}$$

hence $\Delta(\beta_c, N_1, N_2) = \alpha$.

In practice, N is determined by the way we discretize the Brillouin zone in Equa-

tion (3.6) and the thermodynamics limit is reached when the sum becomes an integral. We can generate curves $\Delta(\beta, N_1, N_2)$ v.s. β for a few choices of N_1 and N_2, as in Figure B.1. These curves all go through the point (β_c, α).

The β_c here corresponds to the ordering temperature predicted by the method, not the magnetic ordering temperature of the real system, which might undergo a structural transition (usually accompanied by magnetic ordering transition) to relieve the magnetic frustration, or might have a much lower critical temperature because of quantum fluctuations, or might not even have a thermal transition.

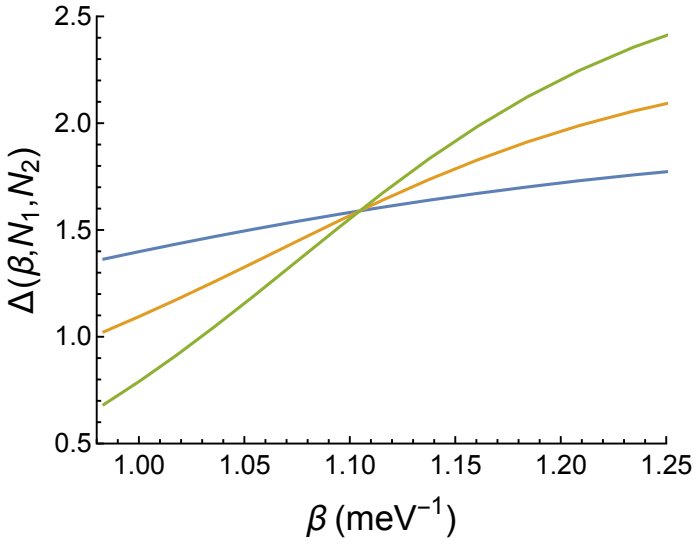

Figure B.1: Finite size scaling to find the theoretical critical temperature in the self-consistent Gaussian approximation. The calculation is performed for the Mott insulator $(V_{1-x}Cr_x)_2O_3$ in the paramagnetic phase with exchange parameters in Reference [93]. The curves focus at $\beta_c \approx 1.1$ meV^{-1} and $\alpha \approx 1.6$, giving a "transition temperature" of approximately 10.5 K, which is much lower than the structural transition temperature in the system.

Bibliography

[1] B. I. Halperin and W. M. Saslow, "Hydrodynamic theory of spin waves in spin glasses and other systems with noncollinear spin orientations," *Phys. Rev. B*, vol. 16, pp. 2154–2162, 1977.

[2] G. H. Wannier, "Antiferromagnetism. The triangular Ising net," *Phys. Rev.*, vol. 79, pp. 357–364, 1950.

[3] P. W. Anderson, "Resonating valence bonds: A new kind of insulator?" *Mater. Res. Bull.*, vol. 8, no. 2, pp. 153 – 160, 1973.

[4] C. Lacroix, P. Mendels, and F. Mila, *Introduction to Frustrated Magnetism.* Berlin, Heidelberg: Springer, 2011.

[5] L. Savary and L. Balents, "Quantum spin liquids," *Rep. Prog. Phys.*, vol. 80, p. 016502, 2017.

[6] J. Knolle and R. Moessner, "A field guide to spin liquids," *Annu. Rev. of Condens. Matter Phys.*, vol. 10, no. 1, pp. 451–472, 2019.

[7] C. Broholm, R. J. Cava, S. A. Kivelson, D. G. Nocera, M. R. Norman, and T. Senthil, "Quantum Spin Liquids," *arXiv:1905.07040*, 2019.

[8] M. Mourigal, M. Enderle, A. Klöpperpieper, J.-S. Caux, A. Stunault, and H. M. Ronnow, "Fractional spinon excitations in the quantum Heisenberg antiferromagnetic chain," *Nat. Phys*, vol. 9, no. 7, pp. 435–441, 2013.

[9] Y. Zhou, K. Kanoda, and T.-K. Ng, "Quantum spin liquid states," *Rev. Mod. Phys.*, vol. 89, p. 025003, 2017.

[10] J. Villain, "Insulating spin glasses," *Z. Phys. B*, vol. 33, no. 1, pp. 31–42, 1979.

[11] S. T. Bramwell and M. J. P. Gingras, "Spin ice state in frustrated magnetic pyrochlore materials," *Science*, vol. 294, no. 5546, pp. 1495–1501, 2001.

[12] B. Canals and D. A. Garanin, "Spin-liquid phase in the pyrochlore antiferromagnet," *Can. J. Phys.*, vol. 79, no. 11-12, pp. 1323–1331, 2001.

[13] J. G. Rau and M. J. P. Gingras, "Frustrated Quantum Rare-Earth Pyrochlores," *Annu. Rev. Condens. Matter Phys*, vol. 10, pp. 357–386, 2019.

[14] M. J. Harris, S. T. Bramwell, D. F. McMorrow, T. Zeiske, and K. W. Godfrey, "Geometrical frustration in the ferromagnetic pyrochlore $Ho_2Ti_2O_7$," *Phys. Rev. Lett.*, vol. 79, pp. 2554–2557, 1997.

[15] A. P. Ramirez, A. Hayashi, R. J. Cava, R. Siddharthan, and B. S. Shastry, "Zero-point entropy in 'spin ice'," *Nature*, vol. 399, pp. 333–335, 1999.

[16] M. Hermele, M. P. A. Fisher, and L. Balents, "Pyrochlore photons: The $U(1)$ spin liquid in a $S = \frac{1}{2}$ three-dimensional frustrated magnet," *Phys. Rev. B*, vol. 69, p. 064404, 2004.

[17] L. Savary and L. Balents, "Coulombic quantum liquids in spin-1/2 pyrochlores," *Phys. Rev. Lett.*, vol. 108, p. 037202, 2012.

[18] A. M. Polyakov, "Quark confinement and topology of gauge theories," *Nuclear Physics B*, vol. 120, pp. 429–458, 1977.

[19] I. F. Herbut, B. H. Seradjeh, S. Sachdev, and G. Murthy, "Absence of U(1) spin liquids in two dimensions," *Phys. Rev. B*, vol. 68, no. 19, p. 195110, 2003.

[20] S. V. Isakov, K. Gregor, R. Moessner, and S. L. Sondhi, "Dipolar spin correlations in classical pyrochlore magnets," *Phys. Rev. Lett.*, vol. 93, p. 167204, 2004.

[21] C. L. Henley, "Power-law spin correlations in pyrochlore antiferromagnets," *Phys. Rev. B*, vol. 71, p. 014424, 2005.

[22] R. Moessner and J. T. Chalker, "Properties of a classical spin liquid: The Heisenberg pyrochlore antiferromagnet," *Phys. Rev. Lett.*, vol. 80, pp. 2929–2932, 1998.

[23] ——, "Low-temperature properties of classical geometrically frustrated antiferromagnets," *Phys. Rev. B*, vol. 58, pp. 12 049–12 062, 1998.

[24] J. W. Cahn and J. E. Hilliard, "Free energy of a nonuniform system. I. Interfacial free energy," *J. Chem. Phys.*, vol. 28, no. 2, pp. 258–267, 1958.

[25] A. Chubukov, "Order from disorder in a kagomé antiferromagnet," *Phys. Rev. Lett.*, vol. 69, pp. 832–835, 1992.

[26] J. D. M. Champion and P. C. W. Holdsworth, "Soft modes in the easy plane pyrochlore antiferromagnet," *Journal of Physics: Condensed Matter*, vol. 16, no. 11, pp. S665–S671, 2004.

[27] P. A. McClarty, P. Stasiak, and M. J. P. Gingras, "Order-by-disorder in the xy pyrochlore antiferromagnet," *Phys. Rev. B*, vol. 89, p. 024425, 2014.

[28] J. Villain, R. Bidaux, J.-P. Carton, and R. Conte, "Order as an effect of disorder," *J. Phys. (Les Ulis, Fr.)*, vol. 41, no. 11, pp. 1263–1272, 1980.

[29] E. F. Shender and P. C. W. Holdsworth, *Order by Disorder and Topology in Frustrated Magnetic Systems*. New York, NY: Springer US, 1996, pp. 259–279.

[30] C. L. Henley, "Ordering due to disorder in a frustrated vector antiferromagnet," *Phys. Rev. Lett.*, vol. 62, pp. 2056–2059, 1989.

[31] J. T. Chalker, *Introduction to Frustrated Magnetism: Materials, Experiments, Theory*. Berlin, Heidelberg: Springer Berlin Heidelberg, 2011, ch. Geometrically Frustrated Antiferromagnets: Statistical Mechanics and Dynamics, pp. 3–22.

[32] L. Balents, "Spin liquids in frustrated magnets," *Nature*, vol. 464, no. 7286, pp. 199–208, 2010.

[33] Y. Iqbal, T. Müller, P. Ghosh, M. J. P. Gingras, H. O. Jeschke, S. Rachel, J. Reuther, and R. Thomale, "Quantum and classical phases of the pyrochlore Heisenberg model with competing interactions," *Phys. Rev. X*, vol. 9, p. 011005, 2019.

[34] Y. Huang, K. Chen, Y. Deng, N. Prokof'ev, and B. Svistunov, "Spin-ice state of the quantum Heisenberg antiferromagnet on the pyrochlore lattice," *Phys. Rev. Lett.*, vol. 116, p. 177203, 2016.

[35] M. Taillefumier, O. Benton, H. Yan, L. D. C. Jaubert, and N. Shannon, "Competing spin liquids and hidden spin-nematic order in spin ice with frustrated transverse exchange," *Phys. Rev. X*, vol. 7, p. 041057, 2017.

[36] R. Rajaraman, *Fractional Charge*. Berlin, Heidelberg: Springer, 2002, pp. 383–399.

[37] L. Savary and L. Balents, "Disorder-Induced Quantum Spin Liquid in Spin Ice Pyrochlores," *Phys. Rev. Lett.*, vol. 118, no. 8, p. 087203, 2017.

[38] R. Moessner and S. L. Sondhi, "Three-dimensional resonating-valence-bond liquids and their excitations," *Phys. Rev. B*, vol. 68, p. 184512, 2003.

[39] O. Benton, O. Sikora, and N. Shannon, "Seeing the light: Experimental signatures of emergent electromagnetism in a quantum spin ice," *Phys. Rev. B*, vol. 86, p. 075154, 2012.

[40] A. Kitaev, "Anyons in an exactly solved model and beyond," *Ann. Phys. (N.Y.)*, vol. 321, no. 1, pp. 2 – 111, 2006.

[41] A. Banerjee, J. Yan, J. Knolle, C. A. Bridges, M. B. Stone, M. D. Lumsden, D. G. Mandrus, D. A. Tennant, R. Moessner, and S. E. Nagler, "Neutron scattering in the proximate quantum spin liquid α-$RuCl_3$," *Science*, vol. 356, no. 6342, pp. 1055–1059, 2017.

[42] Y. Kasahara, T. Ohnishi, Y. Mizukami, O. Tanaka, S. Ma, K. Sugii, N. Kurita, H. Tanaka, J. Nasu, Y. Motome, T. Shibauchi, and Y. Matsuda, "Majorana quantization and half-integer thermal quantum Hall effect in a Kitaev spin liquid," *Nature*, vol. 559, no. 7713, pp. 227–231, 2018.

[43] M. Elhajal, B. Canals, R. Sunyer, and C. Lacroix, "Ordering in the pyrochlore antiferromagnet due to Dzyaloshinsky-Moriya interactions," *Phys. Rev. B*, vol. 71, p. 094420, 2005.

[44] T. Okubo, T. H. Nguyen, and H. Kawamura, "Cubic and noncubic multiple-q states in the Heisenberg antiferromagnet on the pyrochlore lattice," *Phys. Rev. B*, vol. 84, no. 14, p. 144432, 2011.

[45] A. B. Harris, A. J. Berlinsky, and C. Bruder, "Ordering by quantum fluctuations in a strongly frustrated Heisenberg antiferromagnet," *J. Appl. Phys.*, vol. 69, no. 8, pp. 5200–5202, 1991.

[46] C. L. Henley, "Order by disorder and gaugelike degeneracy in a quantum pyrochlore antiferromagnet," *Phys. Rev. Lett.*, vol. 96, p. 047201, 2006.

[47] P. H. Conlon and J. T. Chalker, "Spin dynamics in pyrochlore Heisenberg antiferromagnets," *Phys. Rev. Lett.*, vol. 102, p. 237206, 2009.

[48] P. H. Conlon and J. T. Chalker, "Absent pinch points and emergent clusters: Further neighbor interactions in the pyrochlore Heisenberg antiferromagnet," *Phys. Rev. B*, vol. 81, p. 224413, 2010.

[49] K. A. Ross, L. Savary, B. D. Gaulin, and L. Balents, "Quantum Excitations in Quantum Spin Ice," *Phys. Rev. X*, vol. 1, no. 2, p. 021002, 2011.

[50] A. Abrikosov, L. Gorkov, and I. Dzyaloshinski, *Methods of quantum field theory in statistical physics*. New York, N.Y.: Dover, 1963.

[51] P. M. Chaikin and T. C. Lubensky, *Principles of Condensed Matter Physics*. Cambridge University Press, 1995.

[52] S. Zhang, H. J. Changlani, K. W. Plumb, O. Tchernyshyov, and R. Moessner, "Dynamical structure factor of the three-dimensional quantum spin liquid candidate $NaCaNi_2F_7$," *Phys. Rev. Lett.*, vol. 122, p. 167203, 2019.

[53] H. E. Stanley, "Spherical Model as the Limit of Infinite Spin Dimensionality," *Phys. Rev.*, vol. 176, pp. 718–721, 1968.

[54] U. Hizi and C. L. Henley, "Effective hamiltonians for large-spyrochlore antiferromagnets," *J. Phys. Condens. Matter*, vol. 19, no. 14, p. 145268, 2007.

[55] P.-H. Chavanis, "Generalized thermodynamics and fokker-planck equations: Applications to stellar dynamics and two-dimensional turbulence," *Phys. Rev. E*, vol. 68, p. 036108, 2003.

[56] P.-H. Chavanis, "Generalized Fokker-Planck equations and effective thermodynamics," *Physica A*, vol. 340, no. 1, pp. 57–65, 2004.

[57] L. R. Walker and R. E. Walstedt, "Computer model of metallic spin-glasses," *Phys. Rev. B*, vol. 22, pp. 3816–3842, 1980.

[58] A. G. D. Maestro and M. J. P. Gingras, "Quantum spin fluctuations in the dipolar Heisenberg-like rare earth pyrochlores," *J. Phys. Condens. Matter*, vol. 16, no. 20, p. 3339, 2004.

[59] K. W. Plumb, H. J. Changlani, A. Scheie, S. Zhang, J. W. Krizan, J. A. Rodriguez-Rivera, Y. Qiu, B. Winn, R. J. Cava, and C. L. Broholm, "Continuum of quantum fluctuations in a three-dimensional S = 1 Heisenberg magnet," *Nat. Phys.*, vol. 15, pp. 54–59, 2019.

[60] S.-H. Lee, C. Broholm, W. Ratcliff, G. Gasparovic, Q. Huang, T. H. Kim, and S.-W. Cheong, "Emergent excitations in a geometrically frustrated magnet," *Nature*, vol. 418, p. 856, 2002.

[61] K. Kamazawa, S. Park, S.-H. Lee, T. J. Sato, and Y. Tsunoda, "Dissociation of spin objects in geometrically frustrated $CdFe_2O_4$," *Phys. Rev. B*, vol. 70, p. 024418, 2004.

[62] J.-H. Chung, M. Matsuda, S.-H. Lee, K. Kakurai, H. Ueda, T. J. Sato, H. Takagi, K.-P. Hong, and S. Park, "Statics and dynamics of incommensurate spin order in a geometrically frustrated antiferromagnet $CdCr_2O_4$," *Phys. Rev. Lett.*, vol. 95, p. 247204, 2005.

[63] K. Tomiyasu, H. Suzuki, M. Toki, S. Itoh, M. Matsuura, N. Aso, and K. Yamada, "Molecular spin resonance in the geometrically frustrated magnet $MgCr_2O_4$ by inelastic neutron scattering," *Phys. Rev. Lett.*, vol. 101, p. 177401, 2008.

[64] T. Fennell, M. J. Harris, S. Calder, M. Ruminy, M. Boehm, P. Steffens, M. H. Lemée-Cailleau, O. Zaharko, A. Cervellino, and S. T. Bramwell, "Multiple Coulomb phase in the fluoride pyrochlore CsNiCrF6," *Nat. Phys.*, vol. 15, no. 1, pp. 60–66, 2019.

[65] X. Bai, J. A. M. Paddison, E. Kapit, S. M. Koohpayeh, J.-J. Wen, S. E. Dutton, A. T. Savici, A. I. Kolesnikov, G. E. Granroth, C. L. Broholm, J. T. Chalker, and M. Mourigal, "Magnetic excitations of the classical spin liquid $MgCr_2O_4$," *Phys. Rev. Lett.*, vol. 122, p. 097201, 2019.

[66] O. Tchernyshyov, R. Moessner, and S. L. Sondhi, "Order by distortion and string

modes in pyrochlore antiferromagnets," *Phys. Rev. Lett.*, vol. 88, no. 6, p. 067203, 2002.

[67] M. J. P. Gingras and P. A. McClarty, "Quantum spin ice: a search for gapless quantum spin liquids in pyrochlore magnets," *Rep. Prog. Phys.*, vol. 77, no. 5, p. 056501, 2014.

[68] A. Banerjee, S. V. Isakov, K. Damle, and Y. B. Kim, "Unusual liquid state of hard-core bosons on the pyrochlore lattice," *Phys. Rev. Lett.*, vol. 100, p. 047208, 2008.

[69] R. Moessner, S. L. Sondhi, and M. O. Goerbig, "Quantum dimer models and effective hamiltonians on the pyrochlore lattice," *Phys. Rev. B*, vol. 73, p. 094430, 2006.

[70] M. J. Harris and M. P. Zinkin, "Frustration in the pyrochlore antiferromagnets," *Mod. Phys. Lett.. B*, vol. 10, no. 10, pp. 417–438, 1996.

[71] J. W. Krizan and R. J. Cava, "$NaCaCo_2F_7$: A single-crystal high-temperature pyrochlore antiferromagnet," *Phys. Rev. B*, vol. 89, p. 214401, 2014.

[72] ——, "$NaCaNi_2F_7$: A frustrated high-temperature pyrochlore antiferromagnet with S=1 Ni^{2+}," *Phys. Rev. B*, vol. 92, p. 014406, 2015.

[73] M. B. Sanders, J. W. Krizan, K. W. Plumb, T. M. McQueen, and C. R. J.,

"$NaSrMn_2F_7$, $NaCaFe_2F_7$, and $NaSrFe_2F_7$: novel single crystal pyrochlore antiferromagnets," *J. of Phys. Cond. Matter*, vol. 29, no. 4, p. 045801, 2017.

[74] T. E. Saunders and J. T. Chalker, "Spin freezing in geometrically frustrated antiferromagnets with weak disorder," *Phys. Rev. Lett.*, vol. 98, p. 157201, 2007.

[75] Y. Cai, M. N. Wilson, A. M. Hallas, L. Liu, B. A. Frand sen, S. R. Dunsiger, J. W. Krizan, R. J. Cava, O. Rubel, Y. J. Uemura, and G. M. Luke, "μSR study of spin freezing and persistent spin dynamics in $NaCaNi_2F_7$," *J. Phys. Condens. Matter*, vol. 30, no. 38, p. 385802, 2018.

[76] P. J. Brown, *International Tables for Crystallography.* Berlin, Heidelberg: Springer, 2006, vol. C.

[77] O. Tchernyshyov and G.-W. Chern, *Introduction to Frustrated Magnetism: Materials, Experiments, Theory.* Berlin, Heidelberg: Springer Berlin Heidelberg, 2011, ch. Spin-Lattice Coupling in Frustrated Antiferromagnets, pp. 269–291.

[78] G.-W. Chern, R. Moessner, and O. Tchernyshyov, "Partial order from disorder in a classical pyrochlore antiferromagnet," *Phys. Rev. B*, vol. 78, p. 144418, 2008.

[79] L. Bellier-Castella, M. J. Gingras, P. C. Holdsworth, and R. Moessner, "Frustrated order by disorder: The pyrochlore anti-ferromagnet with bond disorder," *Can. J. Phys.*, vol. 79, no. 11-12, pp. 1365–1371, 2001.

[80] D. A. Garanin and B. Canals, "Classical spin liquid: Exact solution for the

infinite-component antiferromagnetic model on the kagomé lattice," *Phys. Rev. B*, vol. 59, pp. 443–456, 1999.

[81] C. L. Henley, "The Coulomb phase in frustrated systems," *Annu. Rev. Condens. Matter Phys*, vol. 1, no. 1, pp. 179–210, 2010.

[82] M. P. Zinkin, "Neutron and X-ray scattering studies of Rb_2ZnCl_4, frustrated pyrochlore antiferromagnets, and n_2," *Ph.D. thesis, University of Oxford*, 1996.

[83] B. Canals and C. Lacroix, "Pyrochlore antiferromagnet: A three-dimensional quantum spin liquid," *Phys. Rev. Lett.*, vol. 80, pp. 2933–2936, 1998.

[84] H. Yan, R. Pohle, and N. Shannon, "Half moons are pinch points with dispersion," *Phys. Rev. B*, vol. 98, p. 140402, 2018.

[85] T. Mizoguchi, L. D. C. Jaubert, R. Moessner, and M. Udagawa, "Magnetic clustering, half-moons, and shadow pinch points as signals of a proximate Coulomb phase in frustrated Heisenberg magnets," *Phys. Rev. B*, vol. 98, p. 144446, 2018.

[86] A. L. Chernyshev and M. E. Zhitomirsky, "Spin waves in a triangular lattice antiferromagnet: Decays, spectrum renormalization, and singularities," *Phys. Rev. B*, vol. 79, p. 144416, 2009.

[87] B. Lake, D. A. Tennant, J.-S. Caux, T. Barthel, U. Schollwöck, S. E. Nagler, and C. D. Frost, "Multispinon continua at zero and finite temperature in a near-ideal Heisenberg chain," *Phys. Rev. Lett.*, vol. 111, p. 137205, 2013.

[88] J. W. Krizan and R. J. Cava, "$NaCaNi_2F_7$: A frustrated high-temperature pyrochlore antiferromagnet with S=1 Ni^{2+}," *Phys. Rev. B*, vol. 92, p. 014406, 2015.

[89] T. E. Saunders and J. T. Chalker, "Spin freezing in geometrically frustrated antiferromagnets with weak disorder," *Phys. Rev. Lett.*, vol. 98, p. 157201, 2007.

[90] J. Knolle, D. L. Kovrizhin, J. T. Chalker, and R. Moessner, "Dynamics of a two-dimensional quantum spin liquid: Signatures of emergent majorana fermions and fluxes," *Phys. Rev. Lett.*, vol. 112, p. 207203, 2014.

[91] A. M. Samarakoon, A. Banerjee, S.-S. Zhang, Y. Kamiya, S. E. Nagler, D. A. Tennant, S.-H. Lee, and C. D. Batista, "Comprehensive study of the dynamics of a classical kitaev spin liquid," *Phys. Rev. B*, vol. 96, p. 134408, 2017.

[92] H. Yan, O. Benton, L. Jaubert, and N. Shannon, "Theory of multiple-phase competition in pyrochlore magnets with anisotropic exchange with application to $Yb_2Ti_2O_7$, $Er_2Ti_2O_7$, and $Er_2Sn_2O_7$," *Phys. Rev. B*, vol. 95, no. 9, p. 094422, 2017.

[93] J. C. Leiner, H. O. Jeschke, R. Valentí, S. Zhang, A. T. Savici, J. Y. Y. Lin, M. B. Stone, M. D. Lumsden, J. Hong, O. Delaire, W. Bao, and C. L. Broholm, "Frustrated magnetism in mott insulating $(V_{1-x}Cr_x)_2O_3$," *Phys. Rev. X*, vol. 9, p. 011035, 2019.

Vita

Shu Zhang received her B.S. degree in physics from Tsinghua University, Beijing, China, in 2014. In the same year, she enrolled in the Ph.D. program in Henry A. Rowland Department of Physics and Astronomy at Johns Hopkins University. She was a graduate fellowship at the Kavli Institute for Theoretical Physics in the spring semester, 2019. Starting in September, 2019, she will work as a postdoc in University of California at Los Angeles.